the FEBS Journal

Nucleic acid delivery by cell penetrating peptides derived from dengue virus capsid protein: design and mechanism of action

João M. Freire[1], Ana Salomé Veiga[1], Inês Rego de Figueiredo[1], Beatriz G. de la Torre[2], Nuno C. Santos[1], David Andreu[2], Andrea T. Da Poian[3] and Miguel A. R. B. Castanho[1]

1 Instituto de Medicina Molecular, Faculdade de Medicina, Universidade de Lisboa, Portugal
2 Department of Experimental and Health Sciences, Pompeu Fabra University, Barcelona Biomedical Research Park, Spain
3 Instituto de Bioquímica Médica, Universidade Federal do Rio de Janeiro, Brazil

Keywords
capsid protein; cell penetrating peptide; dengue virus; gene therapy; time-resolved flow cytometry

M. A. R. B. Castanho, Faculdade de Medicina, Instituto de Medicina Molecular, Universidade de Lisboa, Av. Prof. Egas Moniz, Lisboa 1649-028, Portugal
Fax: +351 217999477
Tel: +351 217985136
E-mail: macastanho@fm.ul.pt

(Received 4 July 2013, revised 3 October 2013, accepted 24 October 2013)

doi:10.1111/febs.12587

Cell penetrating peptides (CPPs) can be used as drug delivery systems for different therapeutic molecules. In this work two novel CPPs, pepR and pepM, designed from two domains of the dengue virus (DENV) capsid protein, were studied for their ability to deliver nucleic acids into cells as non-covalently bound cargo. Translocation studies were performed by confocal microscopy in HepG2, BHK and HEK cell lineages, astrocytes and peripheral blood mononuclear cells. Combined studies in HepG2 cells, astrocytes and BHK cells, at 4 and 37 °C or using specific endocytosis inhibitors, revealed that pepR and pepM use distinct internalization routes: pepM translocates lipid membranes directly, while pepR uses an endocytic pathway. To confirm these results, a methodology was developed to monitor the translocation kinetics of both peptides by real-time flow cytometry. Kinetic constants were determined, and the amount of nucleic acids delivered was estimated. Additional studies were performed in order to understand the molecular bases of the peptide-mediated translocation. Peptide–nucleic acid and peptide–lipid membrane interactions were studied quantitatively based on the intrinsic fluorescence of the peptides. pepR and pepM bound ssDNA to the same extent. Partition studies revealed that both peptides bind preferentially to anionic lipid membranes, adopting an α-helical conformation. However, fluorescence quenching studies suggest that pepM is deeply inserted into the lipid bilayer, in contrast with pepR. Moreover, only pepM is able to promote the fusion and aggregation of vesicles composed of zwitterionic lipids. Altogether, the results show that DENV capsid protein derived peptides serve as good templates for novel CPP-based nucleic acid delivery strategies, defining different routes for cell entry.

Introduction

Combining efficacy with target tissue specificity is one of the major challenges in drug delivery, in order to overcome adverse off-target effects to the organism and improve treatment tolerance [1]. In this context,

Abbreviations
alpha-MEM, Minimum essential medium alpha; BHK-21, baby hamster kidney; Chol, cholesterol; CPP, cell penetrating peptide; CPZ, chlorpromazine; DENV C, dengue virus capsid; DMEM, Dulbecco's modified Eagle's medium; DPPC, dipalmitoylphosphatidylcholine; HepG2, Hepatocellular carcinoma; HEK-293T, human embryonic kidney 293T; LUV, large unilamellar vesicle; MBS, membrane-binding sequence; NBD, N-(7-nitrobenz-2-oxa-1,3-diazol-4-yl); 5-NS, 5-doxyl stearic acid; 16-NS, 16-doxyl stearic acid; PBMC, peripheral blood mononuclear cell; POPC, 1-palmitoyl-2-oleoyl-*sn*-glycero-3-phosphocholine; POPE, 1-palmitoyl-2-oleoyl-*sn*-glycero-3-phosphoethanolamine; POPG, 1-palmitoyl-2-oleoyl-*sn*-glycero-3-(phospho-*rac*-(1-glycerol)); POPS, 1-palmitoyl-2-oleoyl-*sn*-glycero-3-phosphoserine; RBS, RNA-binding sequence; RhB, rhodamine-B; RT-FACS, real-time flow cytometry; siRNA, small interfering RNA.

cell penetrating peptides (CPPs) constitute good delivery systems, as shown by a plethora of therapeutic molecules successfully delivered by CPPs for the treatment of multiple diseases [1–3]. CPPs have been widely studied over the last 20 years [4–6] as delivery vectors for diverse biological payloads (e.g. small RNA/DNA, plasmids, antibodies and nanoparticles). Typically, CPPs contain 6–30 amino acid residues, ranging from highly charged (Arg- and Lys-rich sequences) to hydrophobic or amphipathic [4–7] sequences, easily amenable to molecular tuning to achieve high internalization yields [8–10]. Their use in biomedical applications has been extensively evaluated [3,5,11], with a strong focus on their ability to deliver small interfering RNA (siRNA), genes and plasmids of pharmaceutical interest [5,11–14].

Delivering nucleic acids into cells is a difficult task because they are anionic, typically of high molecular weight, and vulnerable to enzymatic degradation. Viral capsid proteins, which naturally pack, protect and deliver the viral genome into cells [10,15], may serve as perfect scaffolds to tackle this problem. However, application of these proteins as drug delivery systems is limited by their size. For instance, dengue virus capsid (DENV C) protein is a 100-amino acid protein occurring as a homodimer [16,17] (Fig. 1A). Therefore, instead of using the whole DENV C protein, we searched for DENV C protein derived peptides, shorter and simpler to produce, to serve as CPP templates. In this work, two such peptides, pepR and pepM (Fig. 1B,C), have been derived from two DENV C protein regions conserved among *Flaviviridae* family members [16,17]: a highly cationic amino acid residue sequence and a hydrophobic one, putatively assigned as RNA-binding and membrane-binding sequences (RBS and MBS respectively; Fig. 1). Besides being conserved, RBS and MBS bear similarities to the Arg-rich and the hydrophobic Pro-rich CPP families, respectively. Furthermore, pepR has previously been shown to interact with membranes and display antimicrobial activity [18].

Concerning the internalization mechanism, a rational combination of biophysical and cellular experiments allows the preferential internalization pathway to be deciphered, which can be by direct membrane translocation or through endocytic routes, such as pinocytosis or dynamin- and clathrin-dependent endocytosis [3]. In this work, both pepR and pepM were used in a systematic study in order to gain insight on the efficacy and mode of action, particularly regarding their potential to deliver nucleic acids (Table S1). A 15-nucleotide ssDNA was used as cargo and the interactions of both free and cargo-complexed peptides with membranes were evaluated. The results showed that pepM enters the cell by direct translocation, whereas pepR uses an endocytic pathway. The development of a real-time flow cytometry (RT-FACS) based protocol allowed an in-depth quantitative study of the kinetics of entry of pepR and pepM, which supported this conclusion. The methodology also constitutes a useful tool for understanding the molecular basis of peptide-mediated membrane translocation of nucleic acids, hence contributing to a more rational and mechanism-based CPP design. Our results reveal that capsid proteins from flaviviruses are rich sources to design and develop new generations of CPPs.

Results

The potential use of pepR and pepM as delivery systems was evaluated through their capacity to translocate nucleic acids across the membranes of different cells using confocal microscopy and flow cytometry. The detailed molecular mechanism of internalization was further explored with lipid vesicles using different biophysical techniques. The rationale of the design of the studies is detailed in Table S1.

Selection and structure of pepR and pepM

DENV C protein is highly charged and its NMR structure revealed four α-helical segments, α_1, α_2, α_3 and α_4 [17]. The protein monomer sequence was analysed with PSIPRED, a secondary structure predictor [19], in order to identify domains with increased ability to behave as CPPs, since most of these peptides have a tendency to form α-helices [4,7,20,21]. The results confirm that the sequences α_1, α_2, α_3 and α_4 have a high

Fig. 1. DENV C protein sequence analysis and design of pepM and pepR. (A) Amino acid sequence of DENV C protein (serotype 2, Puerto Rico 159-S1) highlighting both the hydrophobic and cationic regions: MBS and RBS, respectively. Secondary structure propensity, predicted by PSIPRED, is represented by letter code (c, coil; H, α-helix) and cartoon (ellipse, α-helix). PSIPRED confidence prediction scale bar has four levels (0–25%, 25–50%, 50–75% and 75–100%). (B) 3D representation of DENV C protein (PDB1R6R; left) highlighting the region comprising pepM and pepR (blue) and structural localization of both CPP templates, pepM (green) and pepR (orange), at the DENV C protein monomer structure. (C) Sequence, secondary structure propensity prediction in water and lipid bilayers (using MCPEP [22]) and 3D conformation prediction (using I-TASSER [23]) of pepM (green) and pepR (orange). In (B) and (C), the conformational representations were done with PYMOL software [59]. Positively charged residues (blue), hydrophobic and non-charged residues (red) are highlighted.

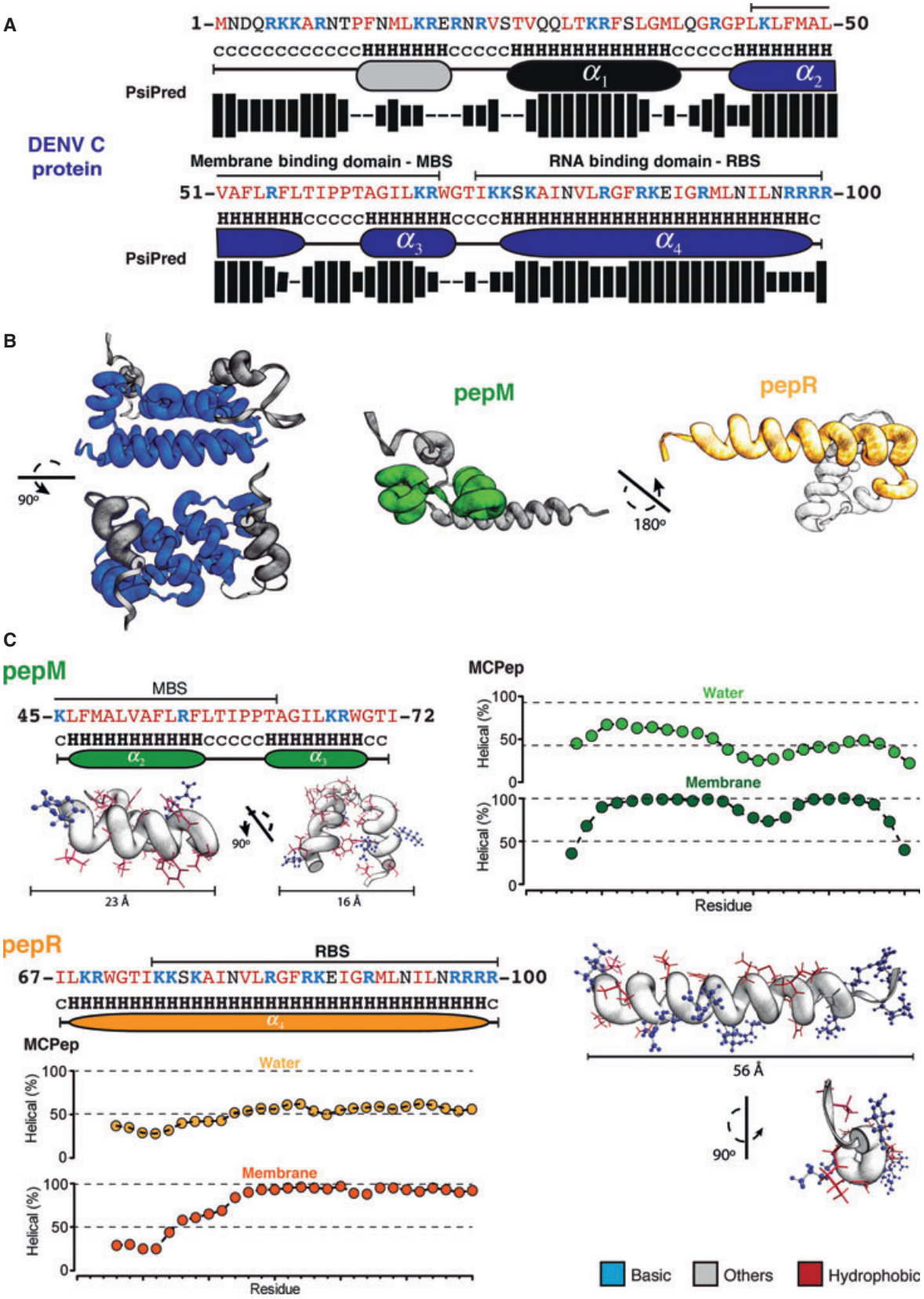
A
1-MNDQRKKARNTPFNMLKRERNRVSTVQQLTKRFSLGMLQGRGPLKLFMAL-50
PsiPred
DENV C protein
Membrane binding domain - MBS
RNA binding domain - RBS
51-VAFLRFLTIPPTAGILKRWGTIKKSKAINVLRGFRKEIGRMLNILNRRRR-100
PsiPred
B
90°
pepM
pepR
180°
C
pepM
MBS
45-KLFMALVAFLRFLTIPPTAGILKRWGTI-72
23 Å
90°
16 Å
MCPep
Water
Membrane
Helical (%)
Residue
pepR
RBS
67-ILKRWGTIKKSKAINVLRGFRKEIGRMLNILNRRRR-100
MCPep
Water
Membrane
Helical (%)
Residue
56 Å
90°
Basic
Others
Hydrophobic

propensity of acquiring α-helical conformation and revealed that the first 20 amino acid residues of DENV C protein, found to be disordered in the NMR studies [17], have moderate α-helical propensity (Fig. 1A). The α_2-α_3 and α_4 are conserved regions [17] and were thus selected as templates for further analyses. These are also the sequences with putative membrane and RNA affinity (highlighted green and orange, respectively, in Fig. 1B,C).

The peptides corresponding to the putative membrane-binding and RNA-binding regions, named pepM (membrane) and pepR (RNA; Fig. 1C), can be assigned to two distinct CPP families [4,5,7]: pepM is highly hydrophobic and contains two Pro residues, which is typical of the hydrophobic/Pro CPP family, and pepR is highly cationic (+12) and fits the requirements of the Arg/Lys-rich CPP family [4,5,7]. MCPEP, a computational tool that estimates the probability of occurrence of secondary structure in peptides (both in aqueous environment and when inserted in lipid bilayers) by Monte Carlo simulation [22], predicts that both peptides acquire a random coil conformation in water. When in membranes, pepM tends to form two α-helices separated by the Pro-rich segment, and pepR tends to form a single long α-helix (Figs 1C and S1). The web server I-TASSER [23] predicted the 3D conformation of both peptides (Fig. 1C). The helical wheel projection of pepR reveals 3D amphipathicity (Fig. S1).

Steady-state fluorescence quenching of Trp residues by acrylamide in aqueous solution [24–26] was performed to evaluate experimentally the solvent exposure of the Trp residue of pepM and pepR (Fig. S2). No significant negative deviation to linearity in the Stern–Volmer plot was observed for the two peptides, showing that Trp residues are exposed to the solvent and suggesting that no significant peptide aggregation occurs in solution. This was corroborated by linear fluorescence intensity versus concentration plots (data not shown), in spite of the higher 3D amphipathicity of pepR relative to pepM.

pepR and pepM are cell penetrating peptides

pepR and pepM labelled with rhodamine-B (RhB) at the N-terminus, non-covalently complexed with an ssDNA oligonucleotide labelled with Alexa-488, were imaged by confocal microscopy in the presence of a panel of very different cells (Fig. 2A,B). Both peptides are generally found in the interior of cells regardless of cell type, which suggests that they do not use specific receptor-mediated mechanisms of entry into cells, leaving endocytosis or direct membrane translocation as possible mechanisms of entry.

Cellular internalization at 37 and 4 °C of pepR, pepM and their ssDNA-Alexa488 cargoes was evaluated by confocal microscopy for a HepG2 cell line and a primary astrocyte culture (Figs 3, 4 and S3–S5). At 4 °C, all metabolic energy-dependent mechanisms (endocytic pathways) are hindered, and direct membrane translocation, when occurring, becomes the dominant mechanism for peptide penetration into cells [3,4]. Figures 2 and 4 show that pepR delivers ssDNA to astrocytes at both temperatures. For HepG2, delivery at 4 °C is nearly absent and at 37 °C most ssDNA is concentrated in the membrane. In contrast to pepR, pepM is able to deliver ssDNA to HepG2 at both temperatures, although the localization differs: ssDNA localizes near the nucleus at 37 °C but not at 4 °C. With astrocytes, pepM does not show internalization of ssDNA regardless of temperature (Figs 2A and 4). It should be stressed that cells were incubated with peptide : ssDNA mixtures having excess peptide. Therefore, the distribution of peptides includes free and complexed peptides. Overall, both pepM and pepR are internalized both at 4 and 37 °C, both by HepG2 cells and astrocytes.

Confocal microscopy results shed light on the cellular localization of labelled peptides and ssDNA cargo but additional data were needed for a complete understanding of the dominant mechanisms of cell penetration used by CPPs. This prompted us to perform quantitative confocal microscopy using endocytosis inhibitors and kinetic studies through RT-FACS. For convenience, BHK-21 cells were chosen for the further steps of the study instead of HepG2 cells, which tend to cluster, thus potentially biasing quantitative results, or astrocytes, which are rather vulnerable to handling in FACS experiments.

Quantitative analysis of pepR and pepM internalization: insights on the endocytic routes used

In addition to the comparative studies at 37 and 4 °C, peptide internalization was also assessed in the presence of two inhibitors of distinct endocytic routes: dynasore, an inhibitor that interferes with all dynamin-dependent endocytic routes [27,28], and chlorpromazine (CPZ), an amphiphilic drug that inhibits clathrin-dependent endocytosis [29,30] (Fig. 5A,B). Figure 5A shows that there is no significant decrease in pepM internalization efficiency when dynasore or CPZ was used. A slight decrease in pepM uptake (1.5-fold) was observed at 4 °C, which may have been caused by a decrease in cell membrane fluidity that slows pepM membrane insertion and translocation. Regarding pepR, the data also confirm the conclusions from pre-

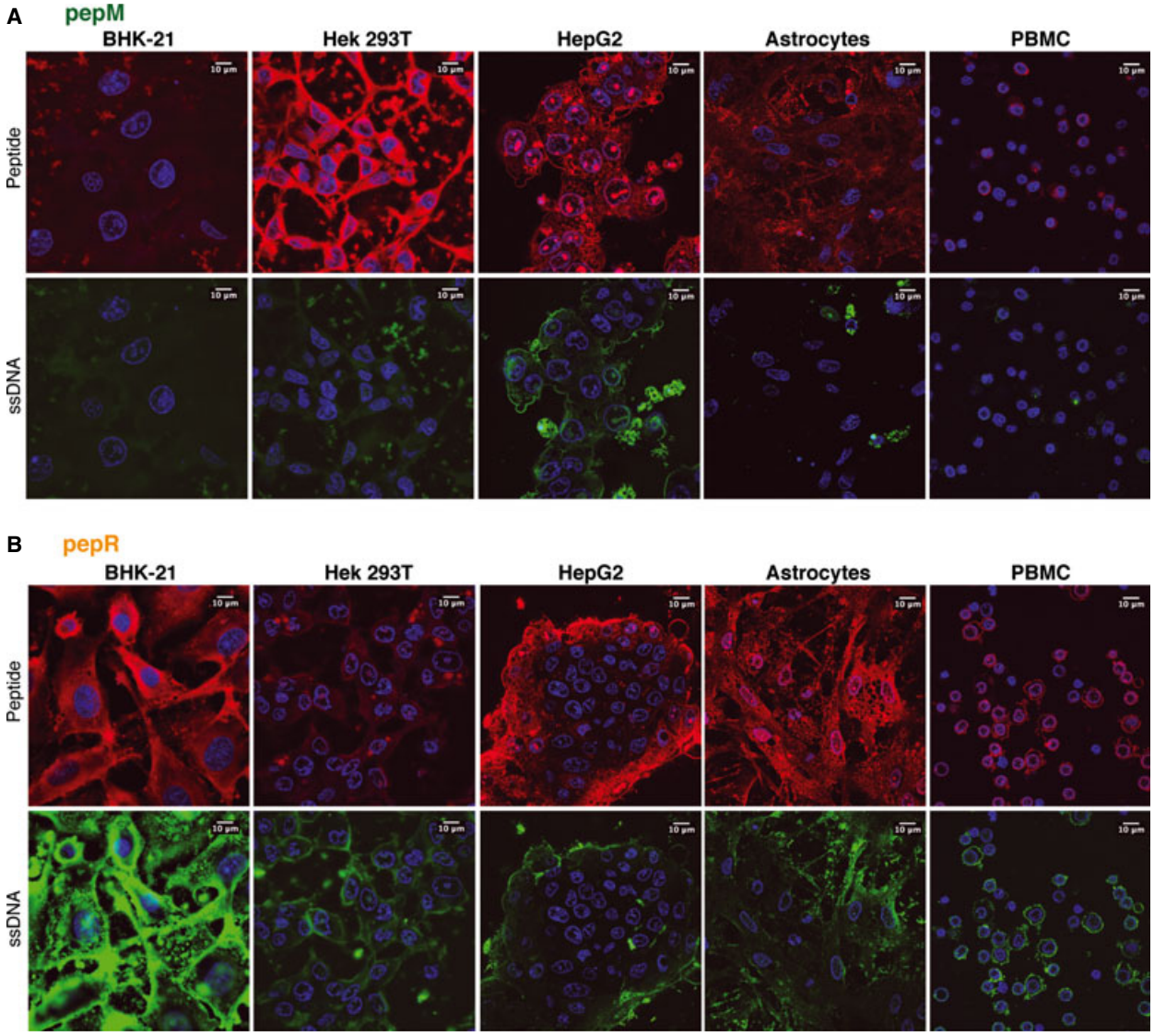

Fig. 2. pepR- and pepM-mediated delivery of ssDNA into cells. Confocal imaging of intracellular delivery of (A) RhB-pepM complexed with ssDNA-Alexa488 and (B) RhB-pepR complexed with ssDNA-Alexa488. Cells were cultured for 2 days and then stained with Hoechst 33342 (nucleus, blue) followed by the addition of 5 μM of either labelled pepR or pepM (red) non-covalently complexed with 1 μM of labelled ssDNA (green).

vious studies on HepG2 cells and astrocytes (Figs 3B and 4B, respectively). Either at 4 °C or in the presence of the inhibitors, there is a significant impairment of pepR uptake by BHK-21 cells compared with the experiments done at 37 °C in the absence of the inhibitors (6-fold decrease). Flow cytometry results further confirm that pepM uses direct membrane translocation as the preferential internalization route, whereas pepR requires endocytic pathways (dynamin- or clathrin-dependent) to reach the interior of cells (Fig. 5B).

Furthermore, the intracellular delivery of peptide : ssDNA complexes was quantified by FACS (Fig. 5C). BHK-21 cells were incubated with the peptide : ssDNA complexes at 4 or 37 °C, and the ssDNA fluorescence signal was recorded after 15 min (Fig. 5C). In agreement with previous results, at 37 °C pepR was able to deliver ssDNA into cells very efficiently (96% of positive cells). Only traces of pepR and ssDNA were observed when the experiment was performed at 4 °C, further confirming that the dominant mechanism for pepR-mediated delivery is endocytosis-dependent. For pepM, the percentages of positive cells at 37 °C were slightly higher than observed at 4 °C, in agreement with the data in Fig. 5A. This

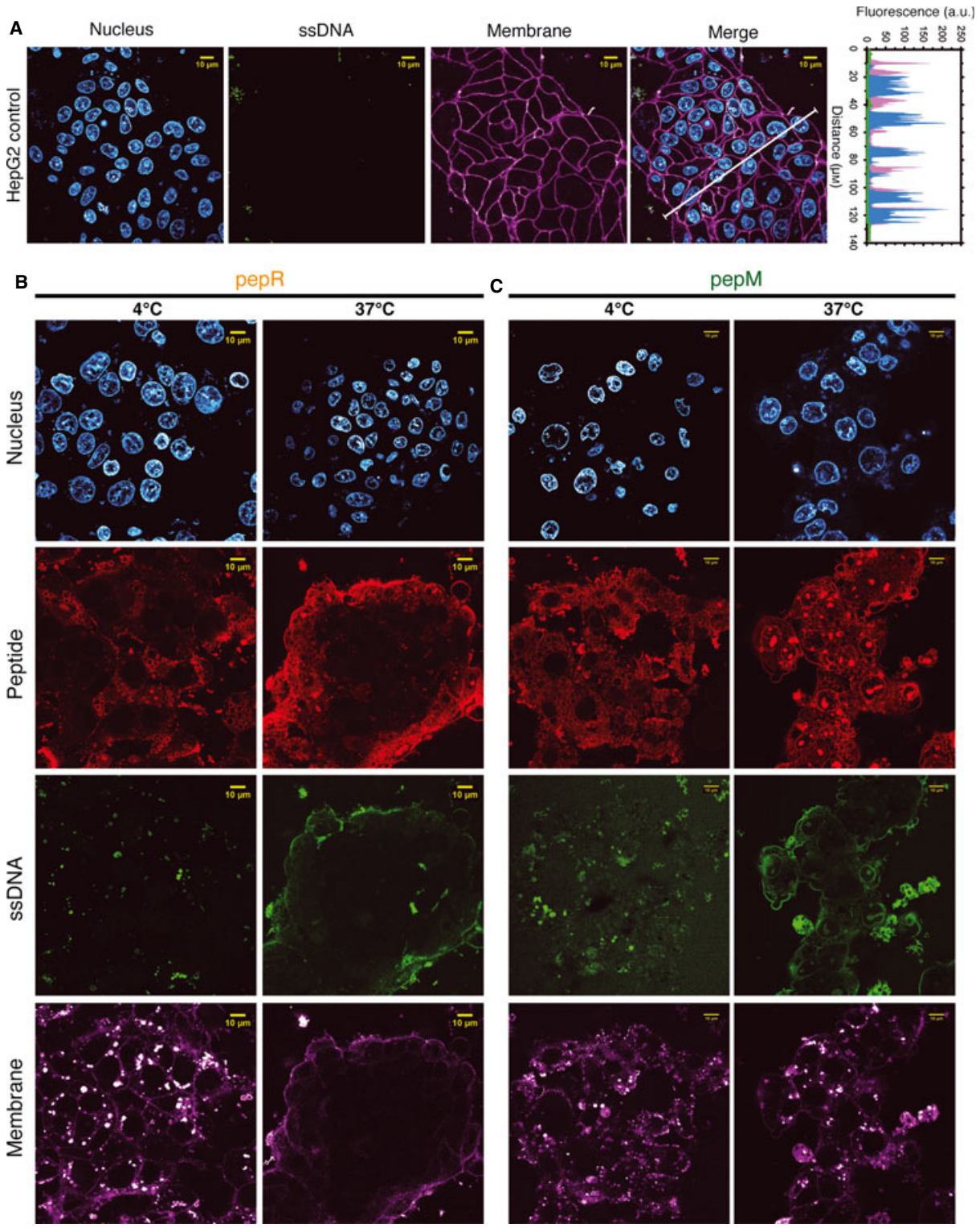

Fig. 3. pepR- and pepM-mediated delivery of ssDNA into HepG2 cells. (A) Confocal imaging of HepG2 cells cultured for 2 days and stained with Hoechst 33342 (nucleus, blue), or Cell Mask Deep Red (membrane, magenta), followed by the addition of 1 μM ssDNA-Alexa488 (green). The fluorescence intensity of each probe along an arbitrary line crossing the image is shown on the right in order to identify the membrane, cytosol and nuclear compartments. (B), (C) Confocal imaging of HepG2 cells, followed by the addition of 1 μM ssDNA-Alexa488 (green) and 5 μM of (B) pepR or (C) pepM labelled with RhB (red) at either 4 or 37 °C.

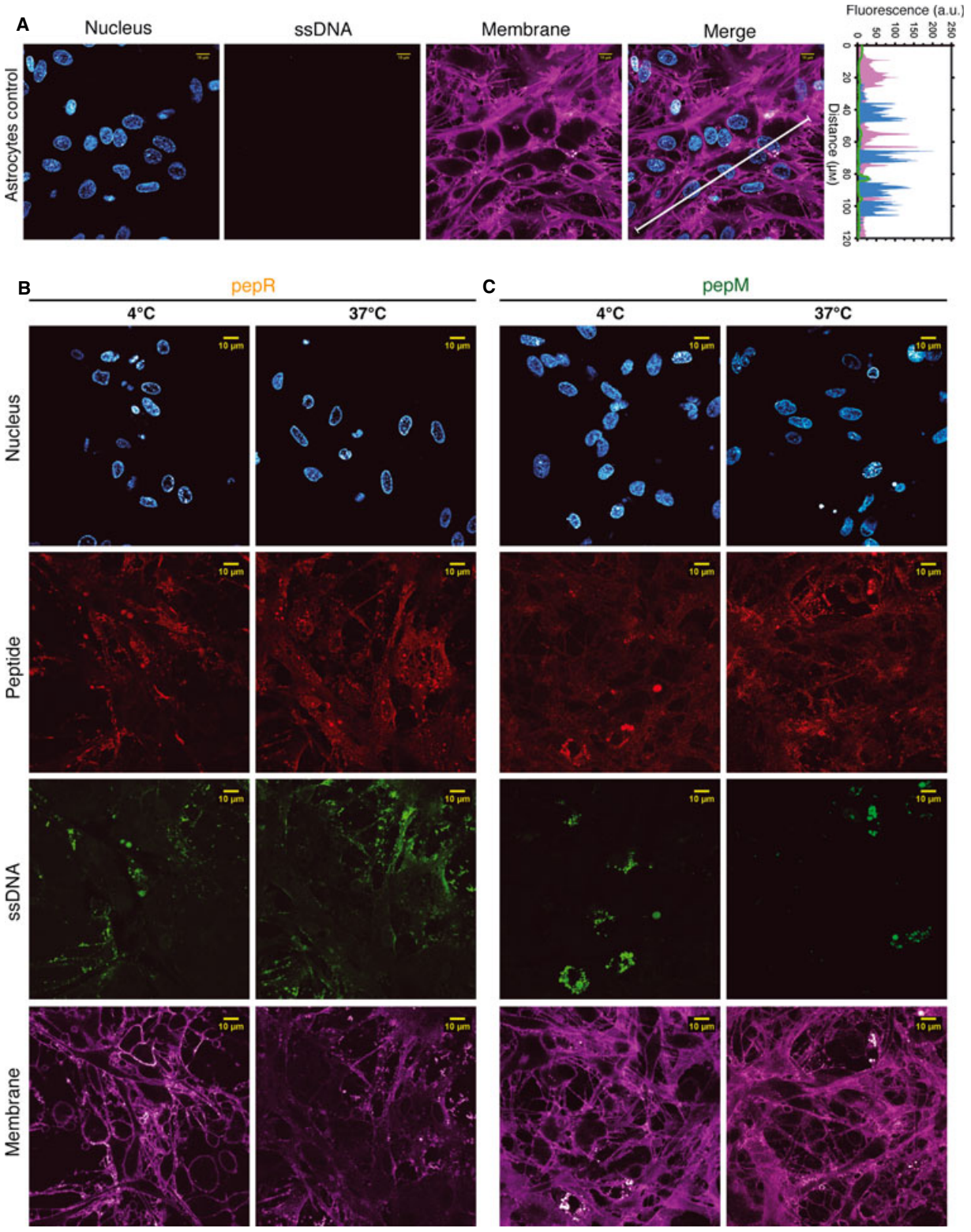

Fig. 4. pepR- and pepM-mediated delivery of ssDNA into astrocytes. (A) Confocal imaging of astrocytes cultured for 2 days and stained with Hoechst 33342 (nucleus, blue) or Cell Mask Deep Red (membrane, magenta), followed by the addition of 1 μM ssDNA-Alexa488 (green). The fluorescence intensity of each probe along an arbitrary line crossing the image is shown on the right in order to identify the membrane, cytosol and nuclear compartments. (B), (C) Confocal imaging of astrocytes, followed by the addition of 1 μM ssDNA-Alexa488 (green) and 5 μM of (B) pepR or (C) pepM labelled with RhB (red) at either 4 or 37 °C.

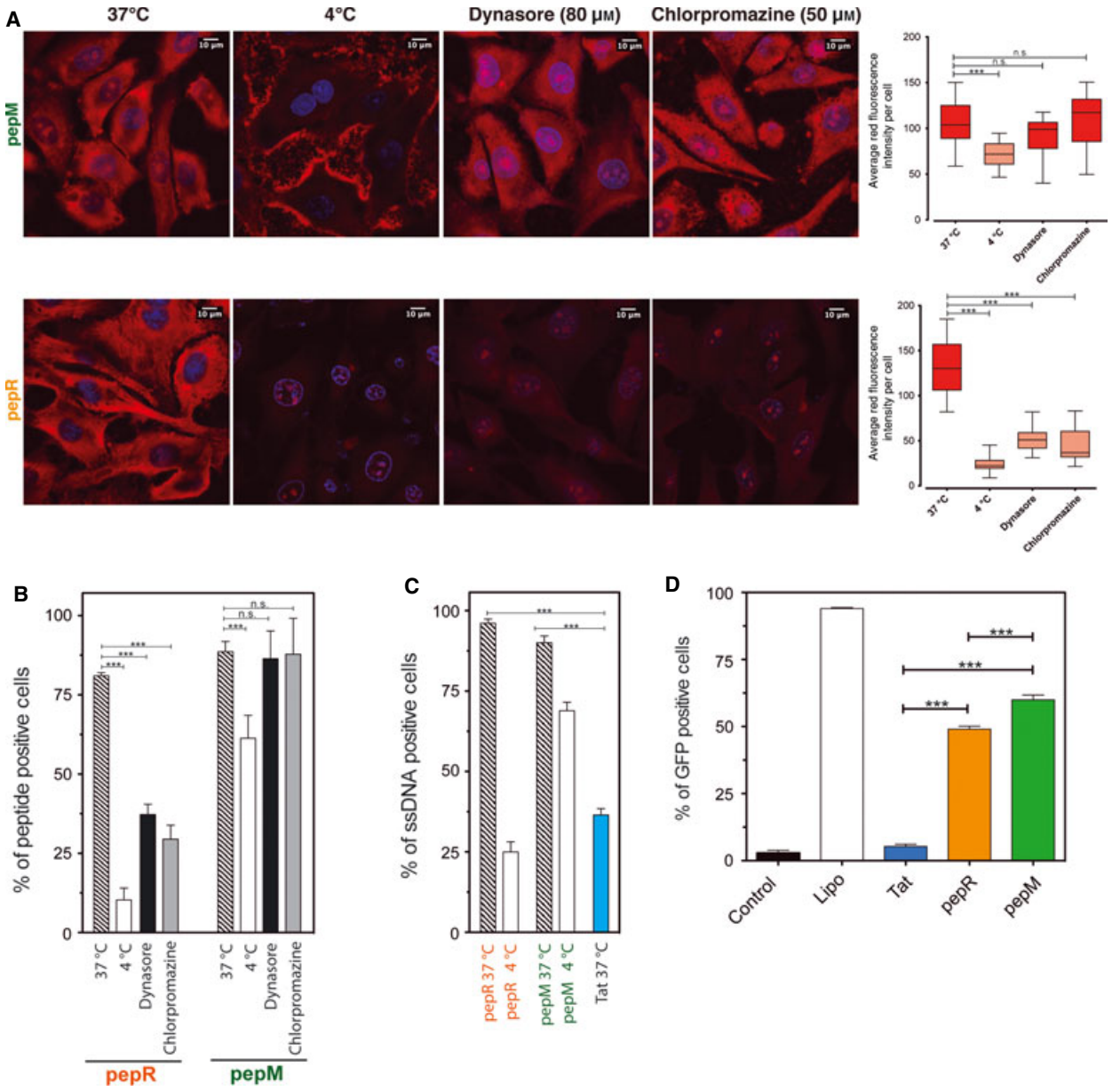

Fig. 5. Screening of RhB-pepR and RhB-pepM cellular internalization routes. (A) Confocal imaging of BHK-21 cells cultured for 2 days and stained with Hoechst 33342 (nuclei, blue), followed by the addition of 5 μM of either RhB-pepM (top panel) or RhB-pepR (bottom panel), at 37, 4 °C or at 37 °C in the presence of the endocytosis inhibitors dynasore (80 μM) or CPZ (50 μM). Laser intensity was kept constant in order to ensure that the fluorescence emission signal reflects the relative proportions of peptide internalization. The fluorescence intensity of each cell in each replicate experiment ($n > 4$, cells > 40) was determined and averaged (right box, whiskers plot). A one-way ANOVA statistical test followed by a Dunnett's test was used to compare each fluorescence signal with the experiments performed at 37 °C in the absence of endocytosis inhibitors (***$P < 0.0001$; n.s., not significant). (B) Percentage of BHK-21 cells positive for RhB-pepR or RhB-pepM, determined by FACS, at 37 °C (dashed), 4 °C (white) and at 37 °C in the presence of the endocytosis inhibitors dynasore (80 μM, black) or CPZ (50 μM, grey). (C) Percentage of BHK-21 cells positive for ssDNA labelled with Alexa488, determined by FACS, at 4 °C (black) and 37 °C (dashed) delivered by 2 μM of pepR or pepM. Delivery with 2 μM of Tat (at 37 °C, blue) was also assayed for comparison with a standard viral CPP. (D) Percentages of GFP-positive cells quantified by flow cytometry after transfection of pEGFP-C3 plasmid using lipofectamine (white), pepR (orange), pepM (green) or Tat (blue; ***$P < 0.001$). BHK cells were cultured for 24 h and transfected with 1 μg of pEGFP-C3 plasmid using either 2 μM of pepR, pepM or Tat, or 4 μL of Lipofectamine 2000. GFP-positive cells were quantified 2 days after transfection.

reinforces the conclusion that this peptide is able to transport cargo into cells through direct plasma membrane translocation. At equimolar concentration Tat, a standard – also virus-derived – CPP [31], is less efficient than pepM or pepR in delivering ssDNA (Fig. 5C).

To evaluate the ability of pepR and pepM to effectively deliver functional cargoes into the cytosol, peptide-mediated transfection of a GFP-encoding plasmid was analysed by quantifying GFP expression in BHK-21 cells using FACS (Figs 5D and S6). Both peptides were able to mediate plasmid transfection with fully functional GFP protein expression, showing that although part of the cargo may locate in the membranes (e.g. pepR-mediated delivery at 37 °C in HepG2 cells – Figs 3 and S4), a significant fraction is efficiently delivered. The fluorescence signal of the labelled peptide persisted up to 48–72 h after transfection (Fig. S6). Both pepR and pepM significantly outperformed Tat in the delivery of both small nucleic acids (Fig. 5C) and large genomes (Fig. 5D), reaching closer to the performance of an artificial transfectant agent such as Lipofectamine used with an optimized protocol (Fig. 5D).

Deciphering the kinetics of CPP cellular entry by RT-FACS

In order to characterize the kinetics of nucleic acid translocation mediated by DENV C protein derived peptides, an RT-FACS methodology was designed and developed (for the experimental rationale and the detailed description of the methodology see Fig. S7 and Materials and methods, respectively). Peptide : ssDNA internalization was monitored as shown in Fig. 6 and Videos S1 and S2. Table 1 shows the kinetic parameters governing the delivery of peptide : ssDNA complexes into BHK-21 cells at 37 and 4 °C. These parameters were obtained by fitting the data using Eqns (4) and (5). The example of pepR : ssDNA mixtures is shown in Fig. 6A and Videos S1 and S2. The cellular average fluorescence intensity for ssDNA and pepR channels at each time point is represented in the top panel. Figure 6A also illustrates the changes in the fluorescence intensity histograms and in the 2D dot plot correlogram (FL1, ssDNA versus FL3, peptide) at times 0, 100, 200, 400 and 600 s (black background and bottom panel). The kinetics of pepR and ssDNA in the mixture differ moderately (Fig. 6A, top panel), as the peptide (2 μM) is in excess over ssDNA (10 nM) in order to achieve complete complexation of the nucleic acid; therefore the output signal of the peptide results from both complexed and free species.

For pepM, internalization starts following a hyperbolic-like function immediately at $t = 0$, both at 37 and 4 °C (Fig. 6B), in clear contrast with pepR (Fig. 6C; Video S3A,B, pepM, and Video S4A,B, pepR). Although a lower final peptide amount inside the cells is attained at 4 °C, as expected from the confocal microscopy and flow cytometry data from Fig. 5, it is clear that translocation occurs, further confirming that pepM is able to translocate cellular membranes directly. For pepR, a biphasic internalization profile at 37 °C was detected, while virtually no uptake is seen at 4 °C (Fig. 6B). The first phase of the internalization process may be assigned to an initial adsorption/concentration of the peptide on the cell surface and recruitment of endocytosis machinery to the membrane. This phase is followed by internalization. The same protocol was performed to analyse the cellular entry of nucleic acid mediated by Tat (Fig. S7). The kinetic profile also revealed an initial lag time for membrane adsorption and subsequent cellular internalization, which agrees with other studies showing that Tat enters cells using endocytic routes [32–35]. In

Table 1. BHK-21 cell entry kinetic parameters. Kinetic rate constant (k_1) of pepR and pepM delivery into BHK-21 cells and time to reach half of the maximum amount delivered ($t_{1/2}$), in the absence (37 or 4 °C) or presence (37 °C to) of ssDNA. These values were obtained using either Eqn (4) (direct translocation) or Eqn (5) (translocation with initial membrane adsorption). Data were obtained from two independent experiments ± standard deviation (SD).

	Peptide cellular internalization kinetics				Peptide : ssDNA complex cellular internalization kinetics (37 °C)				
	4 °C		37 °C		pepR		pepM		Tat
	pepR	pepM	pepR	pepM	Peptide	ssDNA	Peptide	ssDNA	ssDNA
$k_1 \times 10^{-3}$ (s^{-1})	–	5.7 ± 0.2	5.8 ± 0.2	2.5 ± 0.1	0.9 ± 0.02	1.4 ± 0.1	0.78 ± 0.02	0.43 ± 0.01	14.6 ± 1.6
$t_{1/2}$ (s)	–	122	349	278			128	161	148
t_0 (s)	–	–	244	–	250				100
Equation		4	5	4	5	4	4	4	5

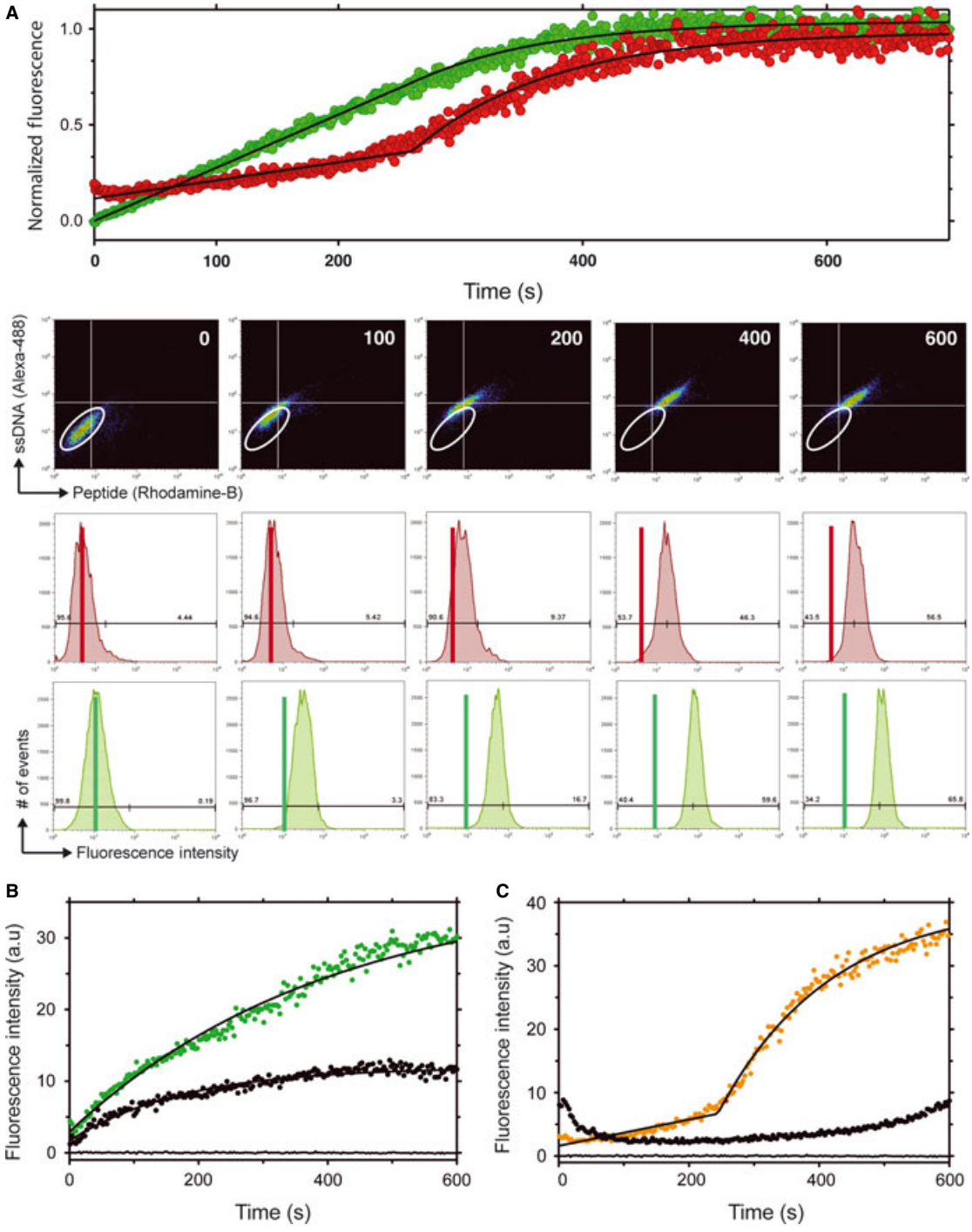

Fig. 6. Kinetics of pepR and pepM cell entry and pepR- and pepM-mediated delivery of ssDNA into BHK-21 cells determined by RT-FACS. (A) RT-FACS of RhB-pepR and ssDNA-Alexa488 cellular internalization at 37 °C. Top: Normalized cellular fluorescence intensity for ssDNA (green) and pepR (red) over time. In order to retrieve the internalization kinetic parameters, Eqns (4) and (5) were used to fit the data (ssDNA and pepR, respectively). Black background correlograms: Flow cytometry snapshots of the time course of the pepR and ssDNA cellular internalization (time frames at 0, 100, 200, 400 and 600 s; ssDNA on *y* axis and pepR on *x* axis. Bottom histograms: pepR (red) and ssDNA (green) fluorescence intensity histograms indicating the percentage of negative and positive cells during internalization. Cell population reference values at $t = 0$ are highlighted with an ellipse in the correlogram and with a red or a green bar in the pepR or ssDNA histograms. Flow cytometry Videos S1 and S2 are available for the real-time internalization of pepM and pepR, respectively. (B), (C) RT-FACS of pepM (B) and pepR (C) cellular internalization at 4 °C (black) and 37 °C (green or orange). See Videos S3 and S4 for temperature internalization assays of pepR and pepM, respectively.

agreement with the steady-state FACS results (Fig. 5C), a lower amount of ssDNA is delivered by Tat compared with pepR or pepM (Table 1).

Molecular basis of pepR and pepM affinity for cargo and lipid membranes

In order to determine the affinities of peptides for both lipid membranes and nucleic acid cargo, fluorescence studies were carried out with unlabelled peptides using the fluorescent properties of their Trp residue [15,24,25,36]. The emission maxima of pepR and pepM occur at 350 and 342 nm respectively in buffer (Fig. 7A,B). The pepR emission maximum coincides with that of free Trp, whereas pepM has a 8 nm blue-shift which suggests that in this peptide the Trp residue is partially shielded from the solvent [25]. The structures predicted for both peptides by MCPEP and I-TASSER (Fig. 1C) are in agreement with these data: in pepM the Trp residue is facing the opposite α-helix, while for pepR the residue is fully exposed to the solvent. When ssDNA or POPC : POPG (4 : 1) large unilamellar vesicles (LUVs) were added to the peptide solution, spectral shifts were observed (Fig. 7A–D), indicating that both pepR and pepM interact with the oligonucleotides or lipids. The complexation of pepM

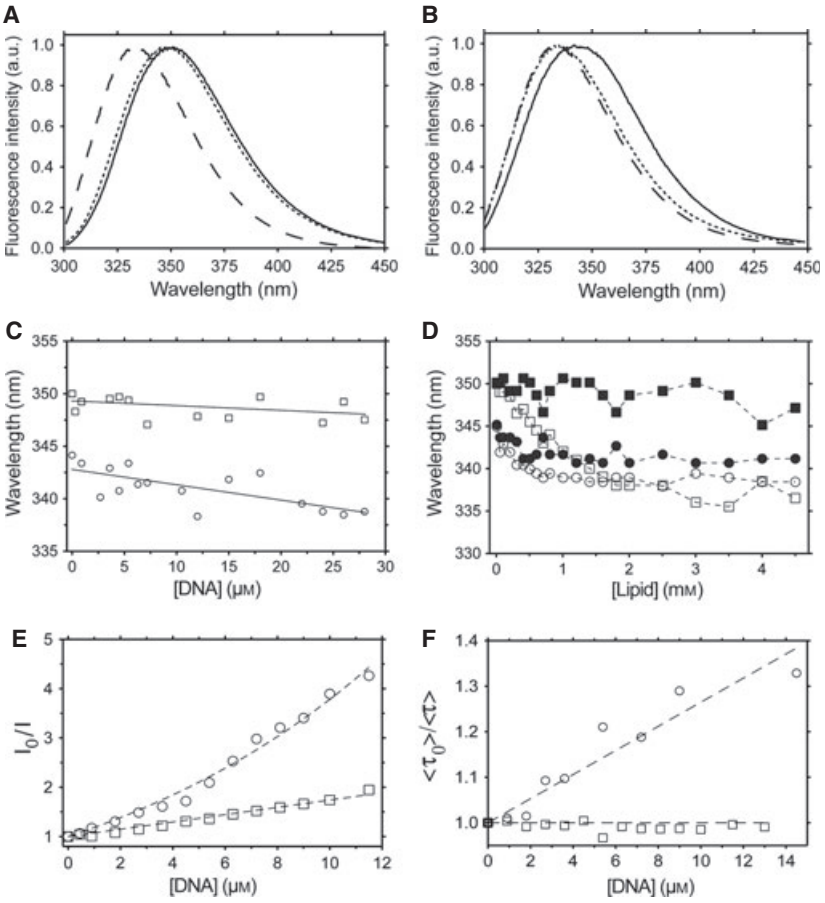

Fig. 7. Spectroscopic analysis of the interaction of pepR and pepM with lipid vesicles or nucleic acids. (A), (B) Normalized Trp fluorescence emission spectra of 36 μM unlabelled pepR (A) or pepM (B) in buffer (solid line), in the presence of 20 μM ssDNA (dotted line) and in the presence of 3 mM POPC : POPG (4 : 1) LUVs (dashed line). (C) Fluorescence emission maximum wavelength of 36 μM unlabelled pepR (squares) and pepM (circles) upon titration with ssDNA. (D) Fluorescence emission maximum wavelength of a 36 μM solution of unlabelled pepR (squares) or pepM (circles) upon titration with POPC LUVs (full squares and circles) or POPC : POPG (4 : 1) LUVs (open squares and circles). (E), (F) Peptide fluorescence quenching by nucleic acids. (E) Stern–Volmer plots of a 36 μM solution of unlabelled pepR (squares) and pepM (circles) upon titration with ssDNA. Equations (6) and (8) were used to fit pepR and pepM data, respectively. (F) Stern–Volmer plots of average fluorescence lifetime obtained from the fluorescence decays of a 36 μM solution of unlabelled pepR (squares) and pepM (circles) upon titration with ssDNA. Equation (12) was used to fit the data to determine the dynamic quenching constant, K_D.

or pepR with ssDNA had different impacts on spectral shifts of the Trp residues (Fig. 7C), which prompted additional experiments.

Nucleic acid binding

Trp fluorescence quenching by nucleic acids [37] was used to quantify the binding of both pepR and pepM to the ssDNA molecule. Both pepR and pepM (at 36 μM) were titrated with ssDNA, and both steady-state fluorescence emission spectra and time-resolved fluorescence emission decays were collected. The linear Stern–Volmer plot obtained with the steady-state fluorescence emission of pepR (Fig. 7E), combined with the absence of collisional quenching (Fig. 7F), show that pepR forms stable complexes with the ssDNA molecules. For pepM, a positive deviation to linearity in the steady-state Stern–Volmer plot was observed (Fig. 7E), which is indicative of simultaneous static and dynamic (collisional) quenching [26,38]. The Stern–Volmer constant of the dynamic process, K_D, was calculated from the data in Fig. 7F using Eqn (12; see Materials and methods). Table 2 summarizes the values obtained for the binding constants of both peptides to ssDNA. The occurrence of collisional quenching for pepM suggests that, in contrast to pepR, the Trp residue is not tightly bound to ssDNA in the inner structure of the peptide : ssDNA complex. A certain degree of motional freedom of the Trp indole group is allowed in pepM, although both peptides have similar affinity for ssDNA [39]. This is in agreement with the more complex structure of pepM relative to pepR (Fig. 1C), accounting for partial protection of the Trp residue in the former peptide.

Partition of free pepR and pepM to lipid membranes

Figure 7D shows the shifts in the maximum wavelength of Trp fluorescence emission spectra of both peptides upon addition of POPC (zwitterionic) and (4 : 1) POPC : POPG (anionic) LUVs. The shift, which is due to peptide insertion in the more hydrophobic environment of the lipid bilayer, was observed for pepR only with anionic LUVs, suggesting that it binds lipid membranes mainly through electrostatic interactions. For pepM, in contrast, spectral shifts were observed with both anionic and zwitterionic LUVs, in agreement with its higher hydrophobicity relative to pepR.

CD studies of both pepR and pepM, in the absence and the presence of (1 : 1) POPC : POPG LUVs, were performed in order to evaluate the changes in peptide secondary structure induced by the interaction with lipid membranes (Fig. 8A,B). In aqueous solution, the spectra of both peptides were characteristic of random coil conformation (minima at 195 nm [40,41]). In the presence of LUVs, spectral signatures characteristic of α-helical peptides were observed, with minima at 208 and 222 nm. The α-helical content, evaluated by the K2D3 on-line server [42], increased in the presence of

Table 2. Peptides and peptide : ssDNA fluorescence quenching parameters.

	Steady state		Time resolved	
	pepR	pepM	pepR	pepM
ssDNA quenching				
K_S (μM^{-1}) × 10^{-2}	7.4 ± 0.2[a]	6.2 ± 1.7	–	–
K_D (μM^{-1}) × 10^{-2}	–	2.3 ± 1.8	0.1 ± 0.03	2.6 ± 0.2
Equation	6	8	12	12
Acrylamide quenching in solution				
K_{SV} (M^{-1})	11.1 ± 0.5	4.8 ± 0.2		
Equation	6	6		
Acrylamide quenching in the presence of lipid vesicles – POPC : POPG (4 : 1)				
K_{SV} (M^{-1})	6.6 ± 4.2	15.8 ± 4.8		
f_B (%)	32.6 ± 14.2	31.4 ± 4.8		
Equation	7	7		
Lipophilic probes 5-NS and 16-NS quenching – POPC : POPG (4 : 1)				
$K_{SV,\ 5\text{-NS}}$ (M^{-1})	3.15 ± 0.11[b]	2.03 ± 0.79		
$K_{SV,\ 16\text{-NS}}$ (M^{-1})	3.40 ± 0.67[c]	0.17 ± 3.86		
$K_{D,\ 5\text{-NS}}$ (M^{-1})			1.32 ± 0.10	2.04 ± 0.05
$K_{D,\ 16\text{-NS}}$ (M^{-1})			1.59 ± 0.07	2.50 ± 0.06
Equation	6[b], 20[c]	20	12	12

[a] In the absence of dynamic quenching, K_{SV} in Eqn (6) can be interpreted as a static (complexation) constant and is thus referred to as K_S.
[b] Eqn (6) was used to fit pepR quenching with 5-NS.
[c] Eqn (20) was used to fit pepR quenching with 16-NS.

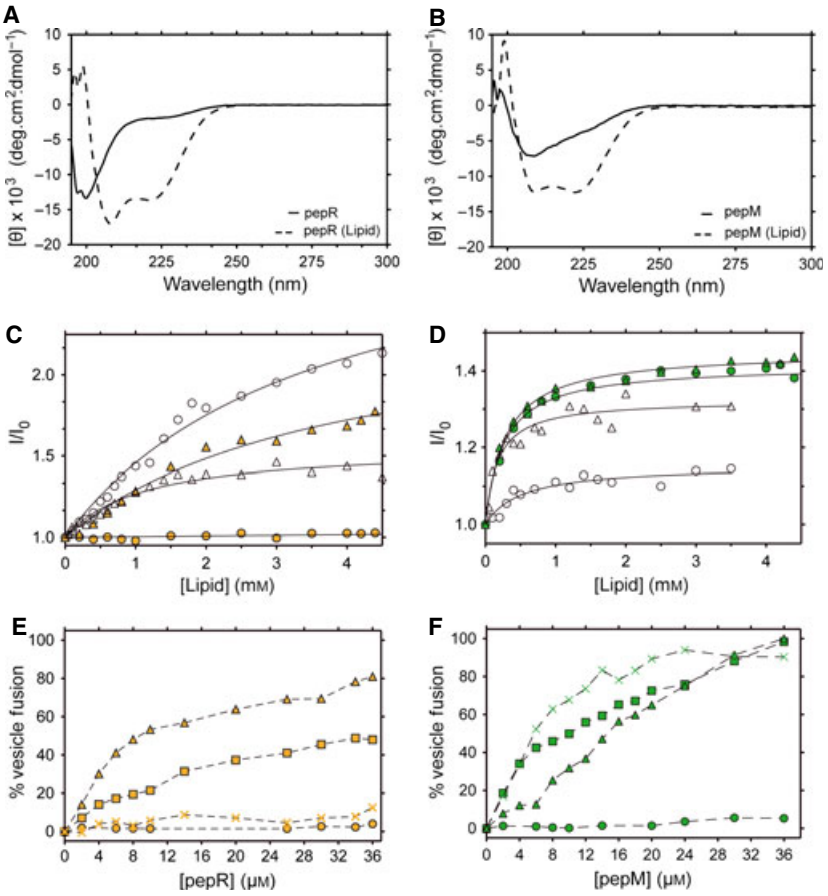

Fig. 8. Conformation of membrane-inserted pepM and pepR and extent of their partition into membranes. (A), (B) CD spectra of 50 μM unlabelled pepM (A) and pepR (B) in buffer (solid line) and in the presence of 3 mM POPC : POPG (1 : 1) LUVs (dashed line). Mean molar residue ellipticity was calculated according to Eqn (13). (C), (D) Membrane partition studies of unlabelled pepR, pepM and their respective unlabelled ssDNA complexes. 36 μM pepR (orange) and pepR : ssDNA (white) (C) or pepM (green) and pepM : ssDNA (white) (D) were titrated with LUVs of POPC (circles) or POPC : POPG (4 : 1; triangles), at pH 7.4. Equation (14) was used to fit the data to obtain the partition constants K_p (Table 3). (E), (F) Membrane fusion caused by pepR (E) or pepM (F). LUVs composed of POPC : POPG 4 : 1 (triangles), POPC : POPS 4 : 1 (squares), POPC (circles) and POPC : POPE 4 : 1 (crosses) were titrated with pepR (orange) or pepM (green) up to 36 μM, at pH 7.4. The percentage of vesicle fusion was calculated using Eqn (17).

LUVs by approximately 10-fold (3.4% to 32.8%) for pepR and 5-fold (3.5% to 16.4%) for pepM. These results are congruent with structural predictions for both pepR and pepM by MCPEP (Fig. 1C). Lipid-membrane-induced acquisition of secondary-level structure in peptides is typical of CPP and other membrane-active peptides [4,7]. Moreover, the CD experimental data and simulations from MCPEP and I-TASSER predict that the peptides in a membrane environment will acquire a structure very similar to that of the homologous regions of DENV C protein.

Differences in 222–208 nm molar ellipticity ratios have been interpreted as evidence of different intrinsic mechanical properties, e.g. elasticity/flexibility, with higher $[\theta]_{222}/[\theta]_{208}$ being indicative of more flexible α-helices [43]. In the presence of LUVs, $[\theta]_{222}/[\theta]_{208}$ values for pepR and pepM were 0.80 and 1.01, respectively, suggesting that, when exposed to lipids, the dynamic structure of pepM is more elastic and flexible than that of pepR.

To further ascertain which lipid composition increased the extent of peptide partition to membranes, the partition constants for both peptides were quantified for several lipid mixtures (Table 3). Peptide preference for liquid disordered (fluid), liquid ordered (raft-like lipid) [44] or rigid gel phase lipid bilayers was evaluated in vesicles constituted by POPC, POPC : Chol (2 : 1) or DPPC, respectively, with both pepM and pepR shown to have a preferential partition to fluid (POPC) LUVs. Additionally, the influence of anionic phospholipids on peptide affinity to lipid membranes was tested on POPC LUVs containing dif-

Table 3. Free pepR and pepM and pepR : ssDNA and pepM : ssDNA partition to lipid vesicles. Partition constants of pepR and pepM, K_p, and of their complexes with ssDNA, $K_{p,C}$, were calculated using Eqn (14). Ratios between the fluorescence intensities in lipid and aqueous solution (I_L/I_W) are also shown in parentheses. Data are presented as the best-fit value ± SD. –, not calculated.

	Partition constant $K_p \times 10^3$ (I_L/I_W)			
	pepR	pepR : ssDNA	pepM	pepM : ssDNA
POPC	~0	0.4 ± 0.1 (3.1 ± 0.2)	5.1 ± 0.7 (1.4 ± 0.0)	2.6 ± 0.7 (1.2 ± 0.0)
DPPC	~0	–	~0	–
POPC : Chol (2 : 1)	~0	–	~0	–
POPC : POPG (4 : 1)	0.4 ± 0.1 (2.4 ± 0.1)	1.2 ± 0.2 (1.6 ± 0.04)	4.6 ± 0.3 (1.5 ± 0.01)	7.6 ± 1.5 (1.3 ± 0.0)
POPC : POPS (4 : 1)	0.2 ± 0.2 (3.1 ± 0.2)	–	2.9 ± 0.3 (1.5 ± 0.0)	–
POPC : POPG (3 : 2)	14.9 ± 1.4 (1.8 ± 0.1)	–	71.4 ± 18.5 (2 ± 0.0)	–
POPC : POPS (3 : 2)	8.2 ± 1.5 (3.4 ± 0.1)	–	2.4 ± 0.7 (1.2 ± 0.0)	–

ferent amounts of POPG or POPS. The titration curves obtained for both pepR and pepM using POPC and POPC : POPG (4 : 1) LUVs are shown as examples in Fig. 8C,D. The combined results show that both pepR and pepM prefer anionic liquid-disordered membranes (Table 3). pepM partitions towards POPC fluid membranes, but the presence of POPG increases K_p from 5×10^3 for pure POPC to 7×10^4 for POPC : POPG (3 : 2). For pepR, anionic lipids are required for peptide partition to membranes. Regarding the preference of the peptides to specific anionic phospholipids, pepM reveals a preference for POPG-rich membranes while for pepR K_p values show that there is no preference for any specific phospholipid anionic head group.

Partition of CPP : ssDNA complexes to lipid membranes

Successful interaction between a CPP–cargo complex and lipid membranes is known to be a crucial element in the design of drug delivery systems [15]: if the complex shows higher membrane affinity the translocation is more likely to occur [45–47]. The results in Figs 2–4 and S3–S5 indicate that the presence of peptide is mandatory for ssDNA interaction with membranes. Therefore, in addition to characterizing free CPP–lipid membrane interaction, it is also important to evaluate the lipid membrane affinity of the CPP–cargo complexes. Since the highest membrane partition of both free peptides was obtained for fluid phase membranes containing anionic lipids (Table 3), POPC and POPC : POPG (4 : 1) LUVs were selected to evaluate the interaction with peptide : ssDNA complexes (Figs 8C,D, S8 and Table 3). The partition constant of the peptide : ssDNA complexes was determined by an extended version [15] of the partition formalism previously developed by us [36,46]. Both pepR : ssDNA and pepM : ssDNA complexes are able to interact with lipid membranes with higher K_p values than those obtained for the respective free peptides in anionic lipid vesicles (Table 3). The pepR : ssDNA complex also partitions to zwitterionic POPC membranes, in contrast to what was observed for the free peptide (Figs 8C, S8A). This result shows that cargo influences the mechanism of action of CPPs [15].

Depth of pepR and pepM insertion into membrane and its impact on lipid organization

The influence of CPPs on membrane organization and the depth of their insertion into lipid bilayers are key issues that determine their efficacy, as well as their mechanism of action and eventual cytotoxicity. In order to evaluate whether pepR and pepM promote LUV aggregation, dynamic light scattering experiments [48,49] were carried out (Figs S9 and S10, respectively). Vesicle aggregation increases the size of the scattering particle in suspension, which is detected by dynamic light scattering. No aggregation was detected for POPC LUVs, whereas POPC : POPG (4 : 1 and 3 : 2) LUVs aggregated in the presence of either pepM and pepR (Figs S9 and S10).

An LUV fusion assay to evaluate whether vesicle aggregation involves membrane fusion showed that it occurred for negatively charged LUVs in the presence of either pepM or pepR (Fig. 8E,F). pepM is highly fusogenic, causing the maximum level of vesicle fusion at 36 μM. Interestingly, it is also able to fuse POPE-rich vesicles (Fig. 8F), which agrees with pepM interaction with zwitterionic lipids, together with the conical shape of POPE, prone to membrane fusion [50].

To study the impact of pepR and pepM on membrane integrity, a leakage assay was performed using POPC, POPC : POPG (4 : 1) and POPC : POPS (4 : 1) LUVs. The fluorescence quenching of LUVs

doped with N-(7-nitrobenz-2-oxa-1,3-diazol-4-yl) (NBD) labelled phospholipids by Co^{2+} ions [51] was tested in the presence of increasing concentrations of either pepM or pepR (Fig. S11). Pore formation related to the presence of peptides would reflect in an increase in NBD quenching efficacy by Co^{2+} (Eqn S1). No pore formation (leakage < 2%) was detected for either peptide in all the lipid systems tested, hence excluding the induction of transient or permanent membrane permeabilization.

Finally, in order to investigate peptide localization in the membrane, the accessibility of the single Trp residue of pepM or pepR to the aqueous quencher acrylamide in the presence of LUVs was also studied (Fig. S2). A more accurate methodology, based on differential fluorescence quenching of two lipophilic doxyl stearic acid probes (5-NS and 16-NS) [52], was used to analyse the in-depth location of such Trp residue in POPC : POPG (4 : 1) LUV (Fig. 9A and 9B for steady-state and time-resolved fluorescence, respectively). Acrylamide quenching experiments showed negative deviations to the Stern–Volmer linearity (Fig. S2), indicating that a fraction of the fluorophore is inaccessible to the aqueous quencher and therefore inserted into the lipid membrane. This accessible fraction, f_B, was determined by applying the Lehrer formalism [24–26] (Eqn 7) to the experimental data (Table 2).

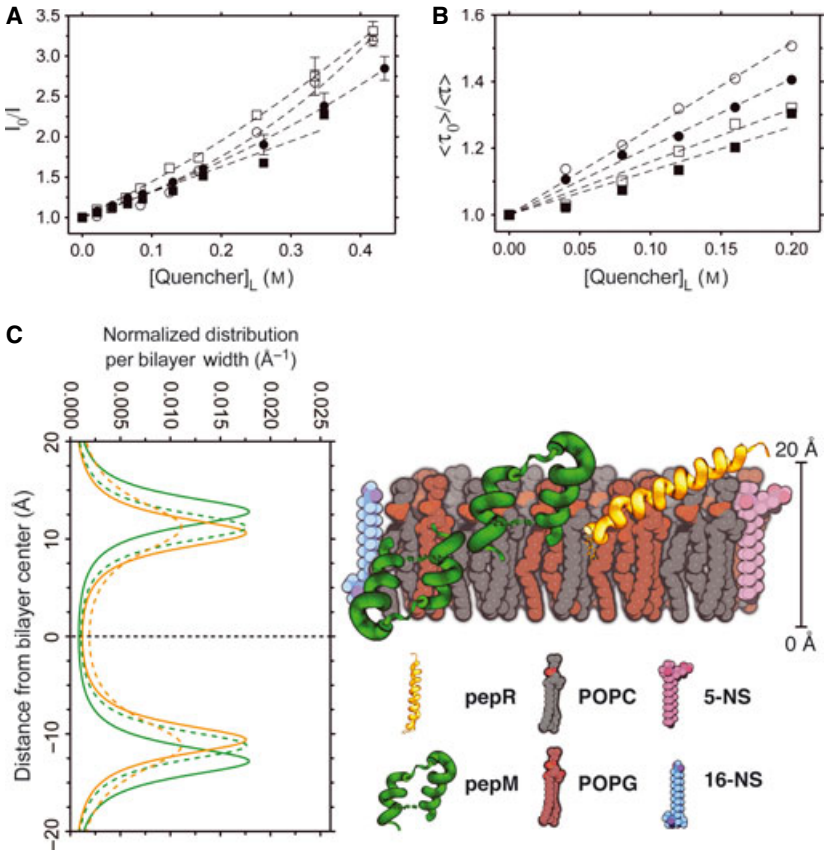

Fig. 9. pepR and pepM depth of insertion into lipid membranes. (A), (B) Stern–Volmer plots of 36 μM unlabelled pepR (squares) and pepM (circles) quenching by 5-NS (solid symbols) or 16-NS (empty symbols), in LUVs of POPC : POPG (4 : 1), using steady-state (A) and time-resolved (B) fluorescence emission data. Quencher concentrations are expressed as effective concentrations in the membrane, determined using Eqn (19). Steady-state data were fitted using either Eqn (6) or Eqn (7), and time-resolved data were fitted using Eqn (12). (C) In-depth localization distribution of the Trp residues of pepM (green) and pepR (orange), obtained by steady-state (solid lines) and time-resolved (dashed lines) data, in POPC : POPG (4 : 1) lipid bilayers, predicted by a method described elsewhere [52]. The cartoon represents the estimated spatial orientation of pepM and pepR in the lipid bilayer, based on the preferred Trp localization: pepM would be completely inserted into the membrane, whereas for pepR only the Trp N-terminal region would be partially inserted into the bilayer, with the C-terminal charged region interacting with the polar head groups of the lipids. The lipophilic probes 5-NS (pink) and 16-NS (purple) are also represented in fully extended conformation.

5- and 16-NS differ only in the position of the doxyl quencher group on the aliphatic chain of stearic acid, resulting in different depths of insertion into lipid bilayers; the closer the Trp residue of either peptide is to the quencher group inside the membrane, the more efficient the quenching and, consequently, the higher the K_{SV} value (Fig. 9A,B and Table 2). Brownian dynamics simulations of quenching agents inside bilayers allow the in-depth distribution of Trp residues to be estimated [52] and hence the peptide location within the lipid membrane. Predictions from both steady-state and time-resolved fluorescence data returned very similar distributions (Fig. 9C): Trp residues in both pepM and pepR were found to be membrane-buried, at 10–12 Å from the bilayer centre. Since in the latter peptide the Trp residue is near the N-terminus, one might envisage pepR adopting a tilted position on the membrane such as that depicted in Fig. 9C, where the Trp residue is buried and the C-terminal is interfacial.

Discussion

The present work describes a stepwise characterization of two novel CPPs, pepM and pepR, derived from the supercharged [53] protein DENV C. We have characterized the molecular bases of CPP–cargo, CPP–membrane and CPP–cargo–membrane interactions, all of them essential for a molecular understanding of the mechanism of action of these peptides. Although pepR is highly cationic and pepM is more hydrophobic, both have high affinity for nucleic acids, adopt α-helical secondary structures upon interacting with lipid membranes and prefer anionic fluid lipid membrane environments. Peptide : ssDNA complexes have higher affinity towards anionic lipid membranes than the free peptides, and the high concentration of peptide and cargo at the membrane level favours cellular internalization.

pepM induces perturbations in the organization of lipid bilayers composed of anionic or neutral conical (PE) phospholipids. These types of lipids favour membrane fusion [50,51,54], which indeed occurs, although no membrane permeabilization was detected. As pepM inserts fairly deeply in the lipid bilayer core, altogether the data support an inverted micelle mechanism for membrane translocation. pepR shows a similar behaviour regarding its interaction with lipid membranes but its ability to induce membrane fusion is lower and depends exclusively on the presence of anionic lipids, also taking place without permeabilization. Peptide localization data suggest that pepR may be tilted in the membrane, with part of its structure bound at the outer membrane leaflet polar region (Fig. 9C), an orientation that does not favour direct membrane penetration. Additionally, the helical structures of pepR and pepM have different mechanical properties. CD data indicate the pepM conformation to be more flexible and dynamic when interacting with lipid, an advantage for a CPP acting by direct translocation.

Confocal microscopy and flow cytometry studies at both 4 and 37 °C and in the presence of endocytosis inhibitors dynasore and CPZ revealed that both CPPs have distinct dominant internalization mechanisms (Fig. 10). pepM translocation is independent of specific receptors or energy-dependent cell entry pathways, suggesting that pepM penetrates fluid membranes through an inverted micelle mechanism. Pore-associated mechanisms may be discarded due to

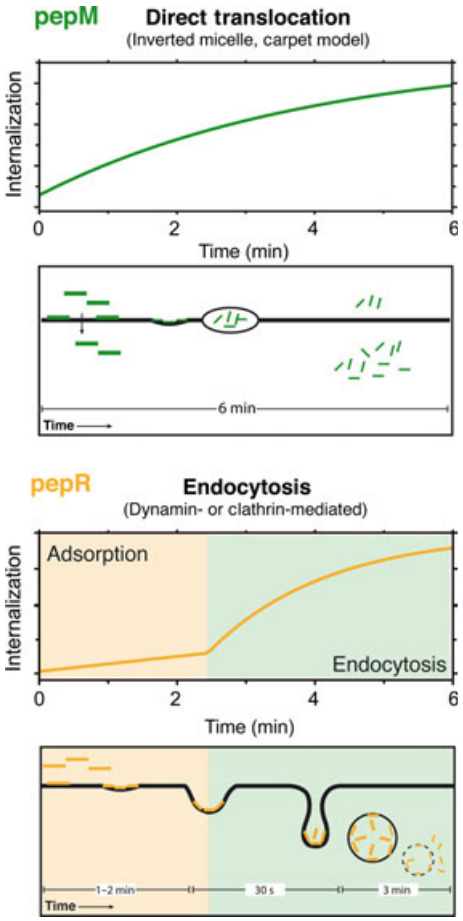

Fig. 10. Schematic representation of the mode of membrane translocation followed by pepM and pepR. pepM (green) uses direct lipid membrane translocation mechanisms, probably the inverted micelle or the carpet model, whereas pepR (orange) internalization is dependent on endocytic pathways, namely dynamin- and clathrin-dependent endocytosis. The results of the present study agree with published data [55] on the time-scale of the events.

the absence of membrane leakage. In contrast, pepR uses dynamin-dependent endocytic pathways, including clathrin-dependent routes, with an initial accumulation at the outer membrane leaflet before internalization. The kinetics of internalization observed by RT-FACS also provided insights on the mechanism of action of pepM and pepR as CPPs. For pepM, kinetics are consistent with direct translocation across the membrane: peptide internalization was observed at both 4 and 37 °C, and the kinetic profile is consistent with a chemical-gradient-driven translocation phenomenon defined by Fick's law of diffusion. pepR displayed a two-step internalization profile, with initial membrane adsorption (linear behaviour) followed by internalization, probably upon reaching the minimum concentration needed at the membrane or recruiting the cellular machinery responsible for endocytosis [55] (Fig. 10). The time-scales, 1–2 min of initial lag and subsequent cellular uptake for the next 30–60 s until maximum, are within the expected values for endocytic pathways, such as clathrin-mediated or pinocytosis [55]. The observation that no significant pepR internalization occurred at 4 °C after 10 min acquisition or in the presence of dynasore or CPZ, except for a constant amount of peptide signal (reflecting the membrane-associated fraction), supports this mechanism.

Concluding remarks

The two CPPs have different biochemical properties and may be considered new members of two different CPP classes [4,5,7]: Arg-rich CPP (pepR) and hydrophobic Pro-rich CPP (pepM). Our study reinforces the idea that the former uses endocytic and the latter non-endocytic mechanisms, thus supporting the view that CPP internalization routes are class-dependent [4]. Regarding cell specificity, our results showed that, although pepM was unable to introduce significant amounts of cargo in primary astrocytes, both peptides translocated and delivered nucleic acids into a wide range of cell types (Fig. 2). This observation raises the hypothesis that some key elements of the cell membrane structure that diverge with cell type and affect bilayer properties [56] are important for CPP function. Primary cell cultures are usually difficult to transfect [12] and it is relevant that pepM and pepR are able to translocate the plasma membrane of astrocytes.

It is worth stressing that the innovative RT-FACS methodology presented here is very informative, simple and effective for studying the internalization mechanism of CPP–cargo complexes as drug delivery systems. In some cases, even for highly efficient CPPs, the CPP–cargo complex is inert and unable to translocate cell membranes [34]. This novel application of FACS, which allows real-time and dynamic analyses of the CPP internalization, is adaptable to high throughput and can be incorporated in the development of drug delivery technologies.

Both pepM and pepR are fragments from two domains of DENV C protein. However, based on the quantitative differences in their translocation abilities, it is reasonable to postulate pepM as a preferential candidate for further development as a gene therapy vector. Structural refinement strategies aimed to improve *in vivo* performance could include, for example, size reduction, D-amino acid insertion to reduce proteolysis, or the insertion of specific homing sequences [1] in order to achieve cell/tissue specificity for therapeutic siRNA delivery. The present work also reveals that structural viral proteins (in this case from the *Flaviviridae* family) may provide excellent scaffolds for CPP design and development.

Materials and methods

Chemicals

Fmoc-protected amino acids were obtained from Senn Chemicals (Dielsdorf, Switzerland) and Fmoc-Rink-amide (MBHA) resin from Novabiochem (Merck, Darmstadt, Germany). 2-(1H-benzotriazol-1-yl)-1,1,3,3-tetramethyluronium hexafluorophosphate (HBTU) and *N*-hydroxybenzotriazole (HOBt) were from Matrix Innovation (Quebec, Canada). HPLC-grade acetonitrile and peptide synthesis-grade *N*,*N*-dimethylformamide, dichloromethane, *N*,*N*-diisopropylethylamine and trifluoroacetic acid were from Carlo Erba-SDS (Sabadell, Spain). Minimum essential medium α (α-MEM), Dulbecco's modified Eagle's medium (DMEM), fetal bovine serum, penicillin-streptomycin (Pen-Strep), phosphate buffered saline (NaCl/P), ssDNA (ACG TGC TGA GCC TAC), ssDNA-Alexa488, the fluorescent dyes Hoechst 33342, Cell Mask Deep Red and 4-[2-[6-(dioctylamino)-2-naphthalenyl]ethenyl]-1-(3-sulfopropyl)-pyridinium (di-8-ANEPPS) were purchased from Life Technologies (Carlsbad, CA, USA). Microscopy ibiTreat coated μ-slide 8μ-well plates were purchased from Ibidi (Munich, Germany). HIV-1 Tat (47–57) was purchased from Bachem (Bubendorf, Switzerland). Dipalmitoylphosphatidylcholine (DPPC), 1-palmitoyl-2-oleoyl-*sn*-glycero-3-phosphocholine (POPC), 1-palmitoyl-2-oleoyl-*sn*-glycero-3-phosphoethanolamine (POPE), 1-palmitoyl-2-oleoyl-*sn*-glycero-3-phosphoserine (POPS), 1-palmitoyl-2-oleoyl-*sn*-glycero-3-(phospho-*rac*-(1-glycerol)) (POPG) and cholesterol (Chol) were obtained from Avanti Polar Lipids (Alabaster, AL, USA). HEPES, NaCl, Triton X-100, 5-doxyl stearic acid (5-NS) and 16-doxyl stearic acid (16-NS) were acquired from Sigma-Aldrich (St Louis, MO,

USA). Acrylamide and L-tryptophan were from Merck. All other reagents were of the highest quality available commercially. All experiments were performed using 10 mM HEPES buffer, pH 7.4, in NaCl 150 mM, unless otherwise stated.

Peptide synthesis

Both pepR (LKRWGTIKKSKAINVLRGFRKEIGRML-NILNRRRR – residues 67–100 of DENV-2 C protein, Fig. 1C) and pepM (KLFMALVAFLRFLTIPPTA-GILKRWGTI – residues 45–72 of DENV-2 C protein, Fig. 1C), as well as their N-terminal RhB-labelled versions, were prepared by solid phase synthesis, as previously described [15,18] (detailed description of synthesis in Data S2; Table S2). Automated syntheses were performed in an ABI433 peptide synthesizer (Applied Biosystems, Carlsbad, CA, USA) running standard Fmoc (FastMoc) protocols [57] at 0.1 mmol scale on Fmoc-Rink-amide MBHA resin. Details on the MALDI-TOF (using a Voyager DE-STR instrument from Applied Biosystems, with an α-hydroxycinnamic acid matrix) and HPLC purification protocols are also available in Figs S12–19. pepR, pepM and their respective fluorescent derivative stock solutions were prepared in Milli Q water.

Peptide computational analysis

For tridimensional structure prediction, the amino acid sequences of pepR and pepM were submitted to the web server I-TASSER [23] (http://zhanglab.ccmb.med.umich.edu/I-TASSER/). For secondary structure propensity prediction, the sequence of DENV C protein [17] (PDB ID 1R6R) was submitted to the web server PSIPRED [19] (http://bioinf.cs.ucl.ac.uk/psipred/), while pepR and pepM sequences were submitted to MCPEP server [22] (http://bental.tau.ac.il/MCPep/index.html). Prediction confidence of the algorithm was represented with a bar scale (higher confidence corresponds to larger bars). Helical wheel projections of pepR and pepM were obtained by the online tool HELIQUEST [58] (http://heliquest.ipmc.cnrs.fr). All molecular measurements and visualizations of proteins, peptides and lipids were done using PYMOL v1.4 [59].

Cell culture

Hepatocellular carcinoma (HepG2) and human embryonic kidney 293T (HEK-293T) cell lines were cultured in DMEM and baby hamster kidney (BHK-21) cell line in α-MEM, both supplemented with 10% (v/v) fetal bovine serum and 100 U·mL^{-1} Pen-Strep, at 37 °C, in a humidified atmosphere of 5% CO_2. Peripheral blood mononuclear cells (PBMCs) were also used due to their relevance in pathological conditions associated with DENV infection, such as leukopenia. To isolate PBMCs, 10 mL of human blood from healthy donors was obtained from the public blood bank Instituto Português do Sangue (Lisbon, Portugal), with their previous informed written consent, as approved by the Ethics Committee of Faculdade de Medicina da Universidade de Lisboa. Blood was drawn to K_3EDTA anticoagulant tubes, and PBMCs were isolated by density gradient using Ficoll-Paque Plus, according to the manufacturer's instructions. Cells were prepared at a final concentration of 1×10^6 cells·mL^{-1} in Pluronic supplemented buffer with 2% fetal bovine serum. Primary cultures of astrocytes were prepared according to Hertz *et al.* [60] and maintained as described elsewhere [61]. Briefly, single cell suspensions obtained from carefully disrupted prefrontal cortex of 1–2-day-old mice brain were plated in culture dishes with DMEM supplemented with 20% (v/v) fetal bovine serum and 10 U·mL^{-1} of Pen-Strep and maintained at 37 °C with 10% CO_2. Cell culture was maintained for 3 weeks at 10% (v/v) fetal bovine serum for full biochemical maturation of the astrocytes.

Cells were counted using a Fuchs–Rosenthal hemocytometer (Brand, Wertheim, Germany) and their viability was determined by the trypan blue dye exclusion method. Viability was always above 98%.

Confocal microscopy

BHK-21, HEK-293T, HepG2 cells, astrocytes or PBMCs were seeded at 4×10^4 cells·mL^{-1} in Ibidi μ-slides and cultured for 2 days. An inverted confocal point-scanning Zeiss LSM 510 META microscope equipped with Diode 405-30, Argon2, DPSS 561-10, HeNe 594 and HeNe 633 lasers and a temperature control incubator (37 °C) with CO_2 supply was used. Images were taken on 8 μ-well slides (Ibidi) with a Plan-Aprochromat 63 × objective (Zeiss, Jena, Germany). Nucleus and cell membrane were stained with Hoechst 33342 (1 mg·mL^{-1}) and Cell Mask Deep Red (50 μg·mL^{-1}), respectively. To each sample, 1 μM of ssDNA-Alexa488 was added, followed by 5 μM of RhB-labelled pepR or pepM. The 4 °C experiments were performed as previously described by Henriques *et al.* [62], and the experiments with the endocytosis inhibitors dynasore or CPZ were performed as described elsewhere [27–30,63]. Briefly, cultured cells were maintained for at least 60 min at 4 °C or 30 min at 37 °C with either dynasore (80 μM) or CPZ (50 μM) prior to ssDNA and peptide additions. Images were taken 15 min later. All images were analysed by the image processor IMAGEJ v1.46 [64]. Co-localization and profile histograms were obtained using the software's incorporated plug-ins. ssDNA–cell membrane co-localization output was used as a negative co-localization control (Figs 3 and 4). The observation of peptide–membrane co-localization with positive peptide : ssDNA overlap is indicative that the ssDNA is located at the cell membrane due to CPP interaction and delivery. One can observe that the ssDNA signal, when in contact with the cell membrane or in the cytosol, is due to peptide action.

GFP plasmid transfection

BHK-21 cells were seeded onto a six-well plate (2×10^5 cells·mL^{-1} in each well) and cultured for 24 h. Then, 1 μg of the pEGFP-C3 plasmid pre-incubated with 2 μM of pepR, pepM or Tat, or 4 μL of Lipofectamine 2000, was added to the cultures. After 6 h, the culture medium was replaced by fresh medium. After 48 h, cells were harvested by trypsinization and washed three times with NaCl/P_i. Transfection was quantified by flow cytometry by following GFP fluorescence emission, recorded for 1 min, using an FL1 detector ($n = 6$).

Flow cytometry

Flow cytometry was performed in a FACScan from BD Biosciences (San Jose, CA, USA) with three detectors: FL1 (530/30 BP), FL2 (585/42 BP) and FL3 (> 670 LP). A suspension of BHK-21 cells (1×10^6 cells·mL^{-1}) was prepared by trypsinization (washed three times with NaCl/P_i). 10 nM of ssDNA labelled with Alexa-488 was added to the medium. Fluorescence intensities in FL1 (Alexa-488) and FL3 (RhB) channels were recorded (10 000 events acquired) 15 min after addition of 2 μM of RhB-pepM, RhB-pepR or Tat. Experiments at 4 °C or with the endocytosis inhibitors were performed as mentioned in the section Confocal microscopy. Fluorescence intensities at the FL1 and FL3 channels were then recorded (10 000 events acquired).

For the kinetic acquisition, the fluorescence in the FL1 and FL3 channels was recorded for 12 min immediately after addition of previously complexed RhB-pepM, RhB-pepR or Tat (2 μM) with 10 nM ssDNA-Alexa488. Before the addition of the complex ($t = 0$), a 30 s acquisition of the fluorescence background of the cellular suspension was performed for further correction in data analysis. After background subtraction, the average fluorescence signal of each channel was plotted versus time of acquisition. The amount of peptide that enters the cell over time was analysed as a kinetic equilibrium described as the passage of the peptide from the aqueous (W) environment to the intracellular (cell) environment:

$$peptide_{\mathrm{W}} \underset{k_{-1}}{\overset{k_1}{\leftrightarrows}} peptide_{\mathrm{cell}} \tag{1}$$

where $k1$ and $k-1$ correspond to the direct and reverse rate constants of the transport process, respectively. Assuming that both processes occur under first-order kinetics and $k-1 \ll k1$ (release of peptides from cells is non-significant), the amount of peptide associated with cells varies over time according to

$$peptide_{\mathrm{Cell}}(t) = peptide_{\mathrm{cell}}(t = \infty)(1 - e^{-k_1 t}) \tag{2}$$

If adsorption phenomena at the cell membrane occur prior to internalization, Eqn (2) is changed to

$$peptide_{\mathrm{cell}}(t) = \begin{cases} m \times t & 0 \le t < t_0 \\ [peptide_{\mathrm{cell}(t=\infty)} - (m \times t_0)] & \\ \quad \times (1 - e^{-k_1(t-t_0)}), & t \ge t_0 \end{cases} \tag{3}$$

The fluorescence intensity signal I, when working on diluted samples, is proportional to the amount of peptide within each environment; therefore Eqns (2) and (3) can be expressed as a function of the fluorescence intensity signal recorded:

$$I_{\mathrm{peptide_{cell}}}(t) = I_{\mathrm{cell_{max}}} \times (1 - e^{-k_1 t}) \tag{4}$$

$$I_{\mathrm{peptide_{cell}}}(t) = \begin{cases} m \times t & 0 \le t < t_0 \\ [I_{\mathrm{cell_{max}}} - (m \times t_0)] \times (1 - e^{-k_1(t-t_0)}), & t \ge t_0 \end{cases} \tag{5}$$

Lipid vesicle preparation

LUVs were used as biomembrane model systems. They typically have approximately 100 nm diameter and were prepared by extrusion, as described elsewhere [65]. Briefly, lipid mixtures were prepared in round glass flasks and dried under vacuum overnight. The solution was then rehydrated and submitted to eight freeze/thaw cycles before performing the extrusion procedure with a 100-nm-pore membrane, using an Avestin LiposoFast Extruder apparatus. Several lipid systems were used, including DPPC, POPC, POPC : Chol (2 : 1), POPC : POPG (4 : 1, 3 : 2 and 1 : 1), POPC : POPS (4 : 1 and 3 : 2) and POPC : POPE (4 : 1).

Fluorescence quenching by acrylamide

Steady-state fluorescence spectra were collected in a FS920 fluorescence spectrophotometer (Edinburgh Instruments, Livingston, UK), equipped with two double monochromators and a 750 W xenon lamp, using excitation and emission slits of 1 and 7 nm, respectively, unless stated otherwise. For pepR and pepM quenching assays, the intrinsic fluorescence of the Trp residue was monitored. Peptide (15 μM) was titrated with acrylamide (0–100 mM) in the absence and presence of 3 mM POPC : POPG (4 : 1) LUVs. Fluorescence emission spectra between 300 and 450 nm ($\lambda_{\mathrm{exc}} = 290$ nm) were recorded after a minimal incubation time of 10 min. Fluorescence spectra were corrected for the dilution during titration as well as inner filter effect at λ_{exc} [24–26]. Quenching data were analysed with the Stern–Volmer formalism [24–26]:

$$\frac{I_0}{I} = 1 + K_{\mathrm{SV}}[\mathrm{Q}] \tag{6}$$

where I and I_0 are the fluorescence intensities of the sample in the presence and absence of quencher, respectively, K_{SV} is the Stern–Volmer constant and [Q] is the concentration

of quencher. When a negative deviation to the Stern–Volmer relationship was observed, the Lehrer equation [24–26] was applied:

$$\frac{I_0}{I} = \frac{1 + K_{SV}[Q]}{(1 + K_{SV}[Q])(1 - f_B) + f_B} \quad (7)$$

where f_B is the fraction of the light emitted by the peptide accessible to the quencher.

Peptide–nucleic acid interactions

The interaction of either pepR or pepM with oligonucleotides was studied using the Trp fluorescence quenching caused by contact with nucleic acids [37]. When a fluorescence quenching process has a static component, this refers to the ground-state complexation of fluorophore (the peptides, in this case) and quencher (ssDNA). If both dynamic (collisional) and static (complexation) components are present, the Stern–Volmer formalism is

$$\frac{I_0}{I} = (1 + K_S[Q]) \times (1 + K_D[Q]) \quad (8)$$

where K_S and K_D are Stern–Volmer constants. K_D refers to dynamic (collisional) events, and K_S is an apparent fluorophore-quencher (peptide : ssDNA) binding constant [26]. To calculate K_S, K_D has to be known. Time-resolved fluorescence spectroscopy was used with the purpose of calculating K_D. As the acquisition time was kept constant throughout the experiments (20 min), the intensity decays were integrated and the ratio of the integrated decays was used to calculate I_0/I:

$$\frac{\int_t I_0(t)}{\int_t I(t)} = \frac{I_0}{I} \quad (9)$$

The decay integral is the total fluorescence emission of the fluorophore during the acquisition time.

A 36 μM solution of pepR or pepM was titrated with ssDNA (up to 14 μM). Fluorescence emission decays were performed in a LifeSpec II apparatus (Edinburgh Instruments), equipped with an Epled-280 (laser of 275 nm with a repeating rate of 200 ns). Fluorescence emission was recorded at 350 nm (emission slits of 23 nm). A 20 ns range was used for decay acquisition, divided into 2048 channels. Signal acquisition duration was set to 20 min. Instrumental response functions were generated from scatter dispersion (glycogen solution; Acros Organics, Geel, Belgium). FAST software (Edinburgh Instruments) was used for data analysis, using a nonlinear least-squares iterative convolution method. Fluorescence decays were analysed using

$$I(t) = \sum \alpha_i e^{t/\tau_i} \quad (10)$$

where α_i are the pre-exponential factors in a multi-exponential intensity decay, and τ_i is the ith component of the excited state fluorescence lifetime [24–26]. The goodness of fit was evaluated from the residuals distribution and the χ^2 value (decay fits with $0.99 < \chi^2 < 1.1$ were accepted).

The Trp fluorescence decay was fitted by a sum of three exponentials [25] and the average lifetime $\langle\tau\rangle$ was determined according to

$$\langle\tau\rangle = \frac{\sum \alpha_i \tau_i^2}{\sum \alpha_i \tau_i} \quad (11)$$

The Stern–Volmer quenching formalism can be applied to time-resolved data as $I_0/I = \langle\tau\rangle_0/\langle\tau\rangle$ [25,26]. The Stern–Volmer constant in this case refers only to dynamic (collisional) phenomena:

$$\frac{\langle\tau\rangle_0}{\langle\tau\rangle} = 1 + K_D[Q] \quad (12)$$

K_D was calculated by fitting Eqn (12) to the data.

Circular dichroism

CD spectra of 50 μM pepR or pepM in buffer (10 mM HEPES, 50 mM NaF, pH 7.4), in the absence or presence of 3 mM POPC : POPG (1 : 1) LUVs, were acquired at 25 °C in the 195–300 nm wavelength range, using 0.1 cm quartz cells, in a JASCO model J-815 spectropolarimeter (Tokyo, Japan). Each final spectrum corresponds to the average of 10 runs, which were subsequently corrected for buffer or LUV baseline. Spectra are plotted as a function of mean molar residue ellipticity [θ] [40] according to the equation

$$[\theta] = \frac{\varepsilon}{aa \times l \times c} \quad (13)$$

where ε is the observed ellipticity, aa is the number of amino acid residues of the peptide sequence, l is the cell path length and c is the molar peptide concentration. Secondary structure contents for pepR and pepM were assessed using the K2D3 software (http://www.ogic.ca/projects/k2d3//index.html) [42].

Membrane partition studies

Membrane partition studies were performed by sequential addition of aliquots of a 15 mM LUV suspension (reaching a final concentration of 4 mM) to a 36 μM pepR or pepM solution. Lipid compositions of POPC, DPPC, POPC : Chol (2 : 1), POPC : POPG (4 : 1 and 3 : 2) and POPC : POPS (4 : 1 and 3 : 2) were used. Fluorescence

emission spectra were collected from 300 to 450 nm (λ_{exc} = 290 nm; excitation and emission slits of 1 and 7 nm, respectively), allowing 10 min incubation before each measurement. Spectra were corrected for dilution and light scattering effects [66]. The partition constant K_p [36,46] was used to quantify the peptide–lipid affinity and was calculated by fitting the experimental data with

$$\frac{I}{I_W} = \frac{1 + K_P \gamma_L \frac{I_L}{I_W}[L]}{K_P \gamma_L [L]} \quad (14)$$

where I_W and I_L correspond to the maximum value of the fluorescence intensity in the integral (300–450 nm) spectra of the fluorophore in aqueous solution and in the lipid environment, respectively, γ_L is the molar volume of lipid [67] and [L] is its concentration. For each lipid mixture, the fraction of peptide that interacts with the lipid, X_L, can be calculated as

$$X_L = \frac{K_P \gamma_L [L] \frac{I_L}{I_W}}{1 + K_P \gamma_L [L] \frac{I_L}{I_W}} \quad (15)$$

For the peptide complexes, a different formalism was considered. When a peptide : ssDNA complex is formed in the presence of lipid vesicles, the fluorescence intensity signal is

$$I = I_W X_W + I_L X_L + I_{CW} X_{CW} + I_{CL} X_{CL} \quad (16)$$

where I_i and X_i are, respectively, the fluorescence intensity and the molar fraction of peptide in situation i (W, non-complexed in aqueous solution; L, non-complexed in the lipid bilayer; CW, complexed with ssDNA in aqueous solution; CL, complexed with ssDNA in the lipid bilayer). A mathematical model was recently derived to address this situation and it is described in detail elsewhere [15]. It accounts for simultaneous partition of both the free and complexed peptide. In excess ssDNA, all the peptide tends to be complexed, and the partition constant of the complex, $K_{p,C}$, is also retrieved by Eqn (14), in which K_p should be replaced by $K_{p,C}$.

Lipid membrane perturbation assays

Vesicle fusion

The assay is based on the decrease in efficiency of the Förster resonance energy transfer when unlabelled LUVs fuse with labelled LUVs (NBD-PE, donor; RhB-PE, acceptor) [68]. 5 mM of POPC, POPC : POPG (4 : 1), POPC : POPS (4 : 1) or POPC : POPE (4 : 1) LUVs doped with 1% (molar) NBD-POPE and 1% RhB-POPE were prepared and mixed with unlabelled LUVs in a 1 : 4 proportion. The vesicle suspension was then titrated with either pepR or pepM, up to a final concentration of 36 μM. After 15 min incubation, fluorescence emission spectra were collected from 490 to 650 nm (λ_{exc} = 470 nm and both excitation and emission slits of 10 nm). After spectra acquisition, Triton X-100 to a final concentration of 1% (v/v) was added to establish the 100% lipid mixing limit. Peptide fusion efficiency was determined by

$$\%\,fusion\ efficiency = \frac{R_i - R_0}{R_{100\%} - R_0} \quad (17)$$

where R_i, R_0 and $R_{100\%}$ are the ratios of the fluorescence intensity from the donor (NBD) and acceptor (RhB) at the maximum emission wavelengths for each fluorophore at a given concentration of peptide and after Triton X-100 addition, respectively [68].

Dynamic light scattering

Dynamic light scattering experiments were carried out on a Malvern Zetasizer Nano ZS (Malvern, UK) with backscattering detection at 173°, equipped with a He-Ne laser (λ = 632.8 nm) at 25 °C (15 min of equilibration) using disposable polystyrene cells (15 measurements per sample). 50 μM LUV (POPC, and POPC : POPG 4 : 1 and 3 : 2) suspensions were prepared and passed through a 0.45 μm syringe filter. pepR and pepM peptide–lipid ratios varied from 0 to 0.15 and 0.4, respectively. Normalized intensity autocorrelation functions were analysed using the CONTIN method [69,70], retrieving a distribution of diffusion coefficients (D) which can be used for the calculation of the hydrodynamic diameter (D_H) [48,71] through the Stokes–Einstein relationship:

$$D = \frac{kT}{3\pi\eta D_H} \quad (18)$$

where k is the Boltzmann constant, T the absolute temperature and η the medium viscosity. D_H for the sample was determined from the mode of the D distribution.

In-depth membrane localization studies

Membrane depth localization was studied by differential quenching studies [52] involving the sequential addition of a lipophilic quencher – 5- or 16-NS – to a POPC : POPG (4 : 1) LUV suspension (3 mM) previously incubated with 36 μM of either pepR or pepM. Experiments were carried out both in steady state, i.e. acquiring Trp fluorescence spectra from 300 to 450 nm (λ_{exc} = 290), and in time-resolved conditions, i.e. fluorescence decays acquired for each quencher addition (10 min incubation). 5- and 16-NS stock solutions were prepared in ethanol; final ethanol concentrations in vesicle suspensions were kept below 2% (v/v) to prevent bilayer perturbation [72]. Quencher concentrations up to 1.2 mM (relative to total sample volume) were added. The effective quencher concentration at the lipid bilayers, $[Q]_L$, was calculated according to [73]

$$[Q]_L = [Q]_T\left(1 - \frac{K_{p,Q}\gamma_L}{1 - \gamma_L[L] + K_{p,Q}\gamma_L[L]}\right) \times \frac{K_{p,Q}}{1 - \gamma_L[L]} \quad (19)$$

where $[Q]_T$ and $K_{p,Q}$ are, respectively, the total quencher concentration added in the assay and the partition constant of the quencher for the lipid mixture used. The partition constants used for 5- and 16-NS were, respectively, 12 570 and 3340 [74]. Quenching data were analysed using Eqns (6) and (12), as described before. When a positive deviation to the referred formalism was observed, data were interpreted as a quenching sphere-of-action [24–26] in which quenching occurs within a sphere of volume V, centred at the fluorophore, with efficacy γ:

$$\frac{I_0}{I} = (1 + K_{SV}[Q])e^{V[Q]N_A\gamma} \quad (20)$$

Results were further analysed with a methodology based on the knowledge of quencher in-depth membrane distributions, in order to predict peptide distribution in the bilayer [52].

Acknowledgements

This work was supported by Fundação para a Ciência e Tecnologia – Ministério da Educação e Ciência (FCT-MEC, Portugal) (PTDC/QUI-BIQ/112929/2009), by the European Union [projects FP7-PEOPLE IRSES MEMPEPACROSS and FP7-HEALTH-F3-2008-223414 (LEISHDRUG)], by the Spanish Ministry of Economy and Competitiveness (SAF2011-24899), by the Generalitat de Catalunya (2009 SGR 492), by the Brazilian Conselho Nacional de Desenvolvimento Científico e Tecnológico (CNPq), by Fundação Carlos Chagas Filho de Amparo à Pesquisa do Estado do Rio de Janeiro (FAPERJ) and by the National Institute of Science and Technology in Dengue (INCT-Dengue). JMF also acknowledges FCT-MEC for PhD fellowship SFRH/BD/70423/2010. MC acknowledges a grant from Programa Ciência Sem Fronteiras PVE171/2012 (CAPES and CNPq, Brazil). The authors thank Sónia Sá Santos (IMM, Lisbon, Portugal) for the kind gift of the primary astrocyte cultures.

References

1 Svensen N, Walton JGA & Bradley M (2012) Peptides for cell-selective drug delivery. *Trends Pharmacol Sci* **33**, 186–192.
2 Timko BP, Whitehead K, Gao W, Kohane DS, Farokhzad O, Anderson D & Langer R (2011) Advances in drug delivery. *Annu Rev Mater Res* **41**, 1–20.
3 Jarver P, Mäger I & Langel Ü (2010) *In vivo* biodistribution and efficacy of peptide mediated delivery. *Trends Pharmacol Sci* **31**, 528–535.
4 Milletti F (2012) Cell-penetrating peptides: classes, origin, and current landscape. *Drug Discov Today* **17**, 850–860.
5 Bolhassani A (2011) Potential efficacy of cell-penetrating peptides for nucleic acid and drug delivery in cancer. *Biochim Biophys Acta* **1816**, 232–246.
6 Heitz F, Morris MC & Divita G (2009) Twenty years of cell-penetrating peptides: from molecular mechanisms to therapeutics. *Br J Pharmacol* **157**, 195–206.
7 Gautam A, Singh H, Tyagi A, Chaudhary K, Kumar R, Kapoor P & Raghava GPS (2012) CPPsite: a curated database of cell penetrating peptides. *Database* **2012**, bas015.
8 LaManna CM, Lusic H, Camplo M, McIntosh TJ, Barthélémy P & Grinstaff MW (2012) Charge-reversal lipids, peptide-based lipids, and nucleoside-based lipids for gene delivery. *Acc Chem Res* **45**, 1026–1038.
9 Hoyer J & Neundorf I (2012) Peptide vectors for the nonviral delivery of nucleic acids. *Acc Chem Res* **45**, 1048–1056.
10 Wagner E (2012) Polymers for siRNA delivery: inspired by viruses to be targeted, dynamic, and precise. *Acc Chem Res* **45**, 1005–1013.
11 Nguyen J & Szoka FC (2012) Nucleic acid delivery: the missing pieces of the puzzle? *Acc Chem Res* **45**, 1153–1162.
12 Nakase I, Akita H, Kogure K, Gräslund A, Langel Ü, Harashima H & Futaki S (2012) Efficient intracellular delivery of nucleic acid pharmaceuticals using cell-penetrating peptides. *Acc Chem Res* **45**, 1132–1139.
13 Nakase I, Tanaka G & Futaki S (2013) Cell-penetrating peptides (CPPs) as a vector for the delivery of siRNAs into cells. *Mol BioSyst* **9**, 855–861.
14 Lehto T, Kurrikoff K & Langel Ü (2012) Cell-penetrating peptides for the delivery of nucleic acids. *Expert Opin Drug Deliv* **9**, 823–836.
15 Freire JM, Veiga AS & de la Torre BG, Andreu D & Castanho MARB (2013) Quantifying molecular partition of cell-penetrating peptide-cargo supramolecular complexes into lipid membranes: optimizing peptide-based drug delivery systems. *J Pept Sci* **19**, 182–189.
16 Markoff L, Falgout B & Chang A (1997) A conserved internal hydrophobic domain mediates the stable membrane integration of the dengue virus capsid protein. *Virology* **233**, 105–117.
17 Ma L, Jones CT, Groesch TD, Kuhn RJ & Post CB (2004) Solution structure of dengue virus capsid protein reveals another fold. *Proc Natl Acad Sci USA* **101**, 3414–3419.
18 Alves CS, Melo MN, Franquelim HG, Ferre R, Planas M, Feliu L, Bardaji E, Kowalczyk W, Andreu D, Santos NC *et al.* (2010) *Escherichia coli* cell surface perturbation and disruption induced by antimicrobial peptides BP100 and pepR. *J Biol Chem* **285**, 27536–27544.

19 McGuffin LJ, Bryson K & Jones DT (2000) The PSIPRED protein structure prediction server. *Bioinformatics* **16**, 404–405.
20 Henriques ST, Melo MN & Castanho MARB (2006) Cell-penetrating peptides and antimicrobial peptides: how different are they? *Biochem J* **399**, 1.
21 Splith K & Neundorf I (2011) Antimicrobial peptides with cell-penetrating peptide properties and *vice versa*. *Eur Biophys J* **40**, 387–397.
22 Gofman Y, Haliloglu T & Ben-Tal N (2012) Monte Carlo simulations of peptide–membrane interactions with the MCPep web server. *Nucleic Acids Res* **40**, W358–W363.
23 Roy A, Kucukural A & Zhang Y (2010) I-TASSER: a unified platform for automated protein structure and function prediction. *Nat Protoc* **5**, 725–738.
24 Coutinho A & Prieto M (1993) Ribonuclease T1 and alcohol dehydrogenase fluorescence quenching by acrylamide: a laboratory experiment for undergraduate students. *J Chem Educ* **70**, 425.
25 Santos NC & Castanho MARB (2002) Fluorescence spectroscopy methodologies on the study of proteins and peptides. On the 150th anniversary of protein fluorescence. *Trends App Spect* **4**, 113–125.
26 Lakowicz JR (2006) Principles of Fluorescence Spectroscopy, 3rd edn. Springer, Berlin, Germany.
27 Macia E, Ehrlich M, Massol R, Boucrot E, Brunner C & Kirchhausen T (2006) Dynasore, a cell-permeable inhibitor of dynamin. *Dev Cell* **10**, 839–850.
28 Marina-García N, Franchi L, Kim Y-G, Hu Y, Smith DE, Boons G-J & Núñez G (2009) Clathrin- and dynamin-dependent endocytic pathway regulates muramyl dipeptide internalization and NOD2 activation. *J Immunol* **182**, 4321–4327.
29 Ivanov AI (2008) Pharmacological inhibition of endocytic pathways: is it specific enough to be useful? *Methods Mol Biol* **440**, 15–33.
30 Vercauteren D, Vandenbroucke RE, Jones AT, Rejman J, Demeester J, De Smedt SC, Sanders NN & Braeckmans K (2009) The use of inhibitors to study endocytic pathways of gene carriers: optimization and pitfalls. *Mol Ther* **18**, 561–569.
31 Frankel AD & Pabo CO (1988) Cellular uptake of the tat protein from human immunodeficiency virus. *Cell* **55**, 1189–1193.
32 Richard JP (2005) Cellular uptake of unconjugated TAT peptide involves clathrin-dependent endocytosis and heparan sulfate receptors. *J Biol Chem* **280**, 15300–15306.
33 Ter-Avetisyan G, Tünnemann G, Nowak D, Nitschke M, Herrmann A, Drab M & Cardoso MC (2009) Cell entry of arginine-rich peptides is independent of endocytosis. *J Biol Chem* **284**, 3370–3378.
34 Mishra A, Lai GH, Schmidt NW, Sun VZ, Rodriguez AR, Tong R, Tang L, Cheng J, Deming TJ & Kamei DT (2011) Translocation of HIV TAT peptide and analogues induced by multiplexed membrane and cytoskeletal interactions. *Proc Natl Acad Sci USA* **108**, 16883–16888.
35 Madani F, Lindberg S, Langel Ü, Futaki S & Gräslund A (2011) Mechanisms of cellular uptake of cell-penetrating peptides. *J Biophys* **2011**, 414729.
36 Santos NC, Prieto M & Castanho MARB (2003) Quantifying molecular partition into model systems of biomembranes: an emphasis on optical spectroscopic methods. *Biochim Biophys Acta* **1612**, 123–135.
37 Carpenter ML & Kneale GG (1994) Analysis of DNA–protein interactions by intrinsic fluorescence. *Methods Mol Biol* **30**, 313.
38 Castanho MA & Prieto MJ (1998) Fluorescence quenching data interpretation in biological systems. The use of microscopic models for data analysis and interpretation of complex systems. *Biochim Biophys Acta* **1373**, 1–16.
39 Freire JM, Veiga AS, de la Torre BG, Santos NC, Andreu D, Da Poian AT & Castanho MARB (2013) Peptides as models for the structure and function of viral capsid proteins: insights on dengue virus capsid. *Biopolymers* **100**, 325–336.
40 Kelly SM, Jess TJ & Price NC (2005) How to study proteins by circular dichroism. *Biochim Biophys Acta* **1751**, 119–139.
41 Greenfield NJ (1999) Applications of circular dichroism in protein and peptide analysis. *TrAC, Trends Anal Chem* **18**, 236–244.
42 Louis-Jeune C, Andrade-Navarro MA & Perez-Iratxeta C (2011) Prediction of protein secondary structure from circular dichroism using theoretically derived spectra. *Proteins* **80**, 374–381.
43 Tatulian SA (2003) Structural effects of covalent inhibition of phospholipase A2 suggest allosteric coupling between membrane binding and catalytic sites. *Biophys J* **84**, 1773–1783.
44 Simons K & Vaz WLC (2004) Model systems, lipid rafts, and cell membranes. *Annu Rev Biophys Biomol Struct* **33**, 269–295.
45 Sargent DF & Schwyzer R (1986) Membrane lipid phase as catalyst for peptide-receptor interactions. *Proc Natl Acad Sci USA* **83**, 5774–5778.
46 Castanho MARB & Fernandes MX (2005) Lipid membrane-induced optimization for ligand–receptor docking: recent tools and insights for the 'membrane catalysis' model. *Eur Biophys J* **35**, 92–103.
47 Ribeiro M, Melo MN, Serrano ID, Santos NC & Castanho MARB (2010) Drug–lipid interaction evaluation: why a 19th century solution? *Trends Pharmacol Sci* **31**, 449–454.
48 Domingues MM, Santiago PS, Castanho MARB & Santos NC (2008) What can light scattering

spectroscopy do for membrane-active peptide studies? *J Pept Sci* **14**, 394–400.
49 Trivedi VD, Yu C, Veeramuthu B, Francis S & Chang DK (2000) Fusion induced aggregation of model vesicles studied by dynamic and static light scattering. *Chem Phys Lipids* **107**, 99–106.
50 Zimmerberg J & Kozlov MM (2005) How proteins produce cellular membrane curvature. *Nat Rev Mol Cell Biol* **7**, 9–19.
51 Ferre R, Melo MN, Correia AD, Feliu L, Bardaji ER, Planas M & Castanho M (2009) Synergistic effects of the membrane actions of cecropin-melittin antimicrobial hybrid peptide BP100. *Biophys J* **96**, 1815–1827.
52 Fernandes MX, García de la Torre J & Castanho M (2002) Joint determination by Brownian dynamics and fluorescence quenching of the in-depth location profile of biomolecules in membranes. *Anal Biochem* **307**, 1–12.
53 Thompson DB, Cronican JJ & Liu DR (2012) Engineering and identifying supercharged proteins for macromolecule delivery into mammalian cells. *Methods Enzymol* **503**, 293–319.
54 Zimmerberg J & Gawrisch K (2006) The physical chemistry of biological membranes. *Nat Chem Biol* **2**, 564–567.
55 Mooren OL, Galletta BJ & Cooper JA (2012) Roles for actin assembly in endocytosis. *Annu Rev Biochem* **81**, 661–686.
56 Ribeiro MMB, Domingues MM, Freire JM, Santos NC & Castanho MARB (2012) Translocating the blood–brain barrier using electrostatics. *Front Cell Neurosci* **6**, 44.
57 Fields GB & Noble RL (1990) Solid phase peptide synthesis utilizing 9-fluorenylmethoxycarbonyl amino acids. *Int J Pept Protein Res* **35**, 161–214.
58 Gautier R, Douguet D, Antonny B & Drin G (2008) HELIQUEST: a web server to screen sequences with specific alpha-helical properties. *Bioinformatics* **24**, 2101–2102.
59 DeLano W (2008) The PyMOL Molecular Graphics System (DeLano Scientific LLC, Palo Alto, CA). Wiley-Interscience, Hoboken, NJ, USA.
60 Hertz L, Drejer J & Schousboe A (1988) Energy metabolism in glutamatergic neurons, GABAergic neurons and astrocytes in primary cultures. *Neurochem Res* **13**, 605–610.
61 Teixeira AP, Santos SS, Carinhas N, Oliveira R & Alves PM (2008) Combining metabolic flux analysis tools and ^{13}C NMR to estimate intracellular fluxes of cultured astrocytes. *Neurochem Int* **52**, 478–486.
62 Henriques ST, Costa J & Castanho MARB (2005) Translocation of β-galactosidase mediated by the cell-penetrating peptide Pep-1 into lipid vesicles and human HeLa cells is driven by membrane electrostatic potential. *Biochemistry* **44**, 10189–10198.
63 Rodrigues M, de la Torre BG, Andreu D & Santos NC (2013) Kinetic uptake profiles of cell penetrating peptides in lymphocytes and monocytes. *Biochim Biophys Acta* **1830**, 4554–4563.
64 Schneider CA, Rasband WS & Eliceiri KW (2012) NIH Image to ImageJ: 25 years of image analysis. *Nat Methods* **9**, 671–675.
65 Santos NC & Castanho MARB (2002) Lipossomas: a bala mágica acertou? *Quím Nova* **25**, 1181–1185.
66 Ladokhin AS, Jayasinghe S & White SH (2000) How to measure and analyze tryptophan fluorescence in membranes properly, and why bother? *Anal Biochem* **285**, 235–245.
67 Nagle JF & Wiener MC (1988) Structure of fully hydrated bilayer dispersions. *Biochim Biophys Acta* **942**, 1–10.
68 Struck DK, Hoekstra D & Pagano RE (1981) Use of resonance energy transfer to monitor membrane fusion. *Biochemistry* **20**, 4093–4099.
69 Provencher SW (1982) A constrained regularization method for inverting data represented by linear algebraic or integral equations. *Comput Phys Commun* **27**, 213–227.
70 Provencher SW (1982) CONTIN: a general purpose constrained regularization program for inverting noisy linear algebraic and integral equations. *Comput Phys Commun* **27**, 229–242.
71 Santos NC & Castanho MA (1996) Teaching light scattering spectroscopy: the dimension and shape of tobacco mosaic virus. *Biophys J* **71**, 1641–1650.
72 Yamazaki M, Miyazu M, Asano T, Yuba A & Kume N (1994) Direct evidence of induction of interdigitated gel structure in large unilamellar vesicles of dipalmitoylphosphatidylcholine by ethanol: studies by excimer method and high-resolution electron cryomicroscopy. *Biophys J* **66**, 729–733.
73 Castanho M & Prieto M (1995) Filipin fluorescence quenching by spin-labeled probes: studies in aqueous solution and in a membrane model system. *Biophys J* **69**, 155–168.
74 Wardlaw JR, Sawyer WH & Ghiggino KP (1987) Vertical fluctuations of phospholipid acyl chains in bilayers. *FEBS Lett* **223**, 20–24.

Supporting information

Additional supporting information may be found in the online version of this article at the publisher's web site:

Fig. S1. pepR and pepM helical wheel representation.
Fig. S2. pepR and pepM quenching by acrylamide.
Fig. S3. Analyses of pepR and pepM co-localization with cell membrane or ssDNA in HepG2 cells and astrocytes.

Fig. S4. Confocal microscopy cross-section of HepG2 cell images.
Fig. S5. Confocal microscopy cross-section of astrocyte images.
Fig. S6. Peptide fluorescence signal in GFP transfection – flow cytometry histograms.
Fig. S7. RT-FACS of ssDNA delivered by Tat.
Fig. S8. pepR and pepM di-8-ANEPPS-LUV experiments.
Fig. S9. Lipid vesicle aggregation studies by dynamic light scattering for pepR.
Fig. S10. Lipid vesicle aggregation studies by dynamic light scattering for pepM.
Fig. S11. pepR and pepM LUV leakage experiments.
Fig. S12. HPLC elution profile of pepR.
Fig. S13. MALDI-TOF spectrum of pure pepR.
Fig. S14. HPLC elution profile of pepR labelled with RhB (RhB-pepR).
Fig. S15. MALDI-TOF spectrum of pure RhB-pepR.
Fig. S16. HPLC elution profile of pepM.
Fig. S17. MALDI-TOF spectrum of unlabelled pepM.
Fig. S18. HPLC elution profile of pepM labelled with rhodamine B (RhB-pepM).
Fig. S19. MALDI-TOF spectrum of pure RhB-pepM.
Data S1. Rationale of the experimental outline.
Data S2. pepR and pepM syntheses and purification data
Video S1. Real-time flow cytometry for pepM : ssDNA internalization into BHK-21 cells: pepM-mediated delivery.
Video S2. Real-time flow cytometry for pepR : ssDNA internalization into BHK-21 cells: ssDNA delivery by pepR.
Video S3. pepM internalization: (A) 4 °C; (B) 37 °C.
Video S4. pepR internalization: (A) 4 °C; (B) 37 °C.
Table S1. Information provided by biophysical assays with vesicles and by cell biology assays for peptides that use dominantly endocytic or non-endocytic mechanisms of entry into cells.
Table S2. Sequences and molecular weights of pepM, pepR and their fluorescent derivatives.